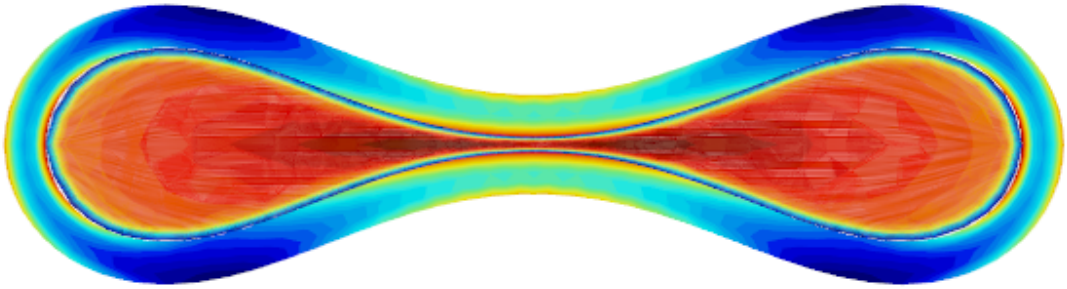

A Chalmers University of Technology Master's Degree project

Fluid-Structure Interaction of Human Upper Airways

Degree project report in Biomedical Engineering

Leandros Papakarmezis

DEPARTMENT OF MECHANICS AND MARITIME SCIENCES

CHALMERS UNIVERSITY OF TECHNOLOGY
Gothenburg, Sweden 2024
www.chalmers.se

Master's Degree project report 2024

Fluid-Structure Interaction of Human Upper Airways

LEANDROS PAPAKARMEZIS

CHALMERS
UNIVERSITY OF TECHNOLOGY

Department of Mechanics and Maritime Sciences
Chalmers University of Technology
Gothenburg, Sweden 2024

Fluid-Structure Interaction of Human Upper Airways
LEANDROS PAPAKARMEZIS

Supervisor: Lukas Schickhofer, Siemens AG
Examiner: Huadong Yao, Mechanics and Maritime Sciences

Master's Degree project report 2024
Department of Mechanics and Maritime Sciences
Chalmers University of Technology
SE-412 96 Gothenburg
Sweden
Telephone +46 31 772 1000

Cover: A collapsed Starling Resistor that models wheezing.

Typeset in LaTeX
Gothenburg, Sweden 2024

Fluid-Structure Interaction Of Human Upper Airways
Leandros Papakarmezis
Department of Mechanics and Maritime Sciences
Chalmers University of Technology

Abstract

This thesis investigates the fluid-structure interaction (FSI) of a Starling Resistor to understand the mechanics behind wheezing, which is a common respiratory symptom. By using a combination of computational fluid dynamics (CFD) and structural analysis, the study applies a partitioned FSI approach to simulate the interaction between airflow and a Starling Resistor. The results of this study present the first valid FSI simulation that models wheezing. In addition, the research investigates how changes in the shape of airways, particularly narrowing in the middle part, affect the flow speed and distribution of pressure. The simulations show how air moves and how the structures change, capture the frequency of the onset of tube's oscillations. The results suggest that the increase in pressure at the inlet of the tube in combination with the external pressure that act on the tube, is the primary mechanism causing the tube's oscillations. This study provides valuable insights into how fluids and structures interact in collapsible airways and contributes to the broader field of respiratory mechanics, especially for wheezing. The results could help in developing better tools for diagnosis and strategies for treating respiratory conditions. Also, future work could focus on improving the simulation models by using more advanced mesh designs, models that account for turbulent flow, finer time steps to accurately capture the exact start and frequency of tube movement and an improvement of signal processing to analyze the tube oscillations with a wavelet process. These improvements could lead to more precise and predictive models, ultimately benefiting both clinical practice and patient diagnoses.

Keywords: wheezing, collapsible tubes, starling resistor, STAR-CCM+, FSI, CFD, Fourier transform, oscillations

Acknowledgements

In truth, I could not have achieved my current level of success without a strong support group and I would like to thank them. First and foremost, my supervisor Lukas Schickhofer for believing in me and offering me this opportunity to do a research in biomechanics, who also was close to me from the fist step of this research as a mentor and colleague and kept me motivated until the end. Last but not least, Huadong Yao as my teacher and examiner, who taught me everything about FSI modeling programs and how to organize and solve problems.

Leandros Papakarmezis, Gothenburg, September 2024

List of Acronyms

Below is the list of acronyms that have been used throughout this thesis listed in alphabetical order:

CFD	Computational Fluid Dynamics
FEM	Finite Element Analysis
FFT	Fourier Transform
FSI	Fluid Structure Interaction
LES	Large Eddy Simulation
Re	Reynolds
SST	Shear Stress Transport
3D	Three Dimensions
2D	Two Dimensions

Nomenclature

Below is the nomenclature of indices, sets, parameters, and variables that have been used throughout this thesis.

Parameters

P_e	External pressure
P_1	Pressure at the inlet
P_2	Pressure at the outlet
l_0	Initial length of tube
l	Length of the tube after stretch
d	Diameter of the tube
h	Thickness of the tube
Q	Average flow rate
E	Young Modulus
v	Poisson's Ratio
ρ_0	Initial density
ρ	Current density
V_0	Initial volume
V	Current volume
d	Displacement
t	Time
b	Total force per unit volume
σ	Cauchy stress tensor
S	Stress tensor
W	Strain energy potential
W_{dev}	Deviatoric part of strain energy potential
W_{vol}	Volumetric part of strain energy potential

μ	Shear modulus, dynamic viscosity
K	Bulk modulus
I_1	The first invariant of the right Cauchy-Green deformation tensor
J	Determinant of the deformation gradient
α_p	Exponent that captures non-linear material behavior
λ_1, λ_2, λ_3	Principal stretches
f_i	Body forces per unit volume
u	Velocity
x	x axis
d_{fluid}	Displacement of fluid
d_{solid}	Displacement of solid
σ_{fluid}	stress tensor in fluid
σ_{solid}	stress tensor in solid
n	Normal vector to the interface
u_{fluid}	Velocity of fluid
u_{solid}	Velocity of solid
M_{MN}	Mass matrix
C_{MN}	Damping matrix
T	Temperature
m_f	Mass flux
$Ppert$	Pressure perturbation
A, B	Perturbation constants
$Ptotal$	Total Pressure

Contents

List of Figures

List of Tables

1
Introduction

1.1 Background

Breathing is essential for human life, yet numerous diseases can negatively impact this vital function. The human upper airways undergo a complex pattern of deformations due to pressure differences between the lungs and the mouth during breathing. These deformations can be influenced by diseases, resulting in lung sounds. These lung sounds are crucial because they offer a low-cost, non-invasive method for diagnosing various pathologies [1]. However, diagnosing diseases based on these sounds remains challenging due to their low specificity [2] and repeatability issues [3][4]. To improve diagnostic accuracy, it is essential to understand the physical mechanisms behind the creation of these sounds, particularly their onset [1].

To model and study the behavior of airways under various conditions, researchers have developed the Starling resistor simplified model of a prestrained, flexible tube. Recent reviews and studies have expanded our understanding of Starling resistors and fluid dynamics in flexible tube [5], [6], [7], [8]. However, most experiments have used water instead of air, which affects the density ratio between fluid and tube walls, making them less relevant for lung studies. The complexity of theoretical models has increased over time. Early work started with two-dimensional analogues of the Starling resistor, exploring both linear stability [9],[10],[11],[12] and direct numerical simulations [13],[14],[15]. Significant progress has been made in advancing our theoretical understanding of Starling resistors, resulting in the development of numerous potential mechanisms. However, until recently, these mechanisms have not allowed for quantitative predictions of the frequencies and flow rates at onset within the specific context of the lung, with one notable exception [16].

One of the most significant lung sounds, affecting 25% of the population, is wheezing [2]. Research has shown that the frequencies of wheezing are not influenced by the density of the fluid, ruling out mechanisms based on the resonance of the air cavity [17]. Additionally, it has been demonstrated that a dog's trachea began to oscillate and produced wheezing sounds when air was sucked through it [18]. This indicates that wheezing is generated by the oscillations of a flexible tube when air passes through it [19]. Recent research suggests that the onset of these oscillations is driven by a complex interplay of fluid dynamics and tube deformation, marked by critical changes in pressure and flow conditions that lead to instability and subsequent oscillatory behavior [16].

1.2 Purpose

The primary purpose of this thesis is to develop and validate a functional FSI setup, beginning with an existing baseline model of the Starling resistor, which undergoes various stages from buckling and flow limitation to complete collapse as upstream pressure, external pressure, and downstream pressure are varied. Figure 1.1 shows flow limitation and complete collapse. Flow limitation occurs when the external pressure exceeds the internal pressure at the outlet, while complete collapse occurs when the external pressure is greater than the pressure at both the inlet and the outlet of the tube.

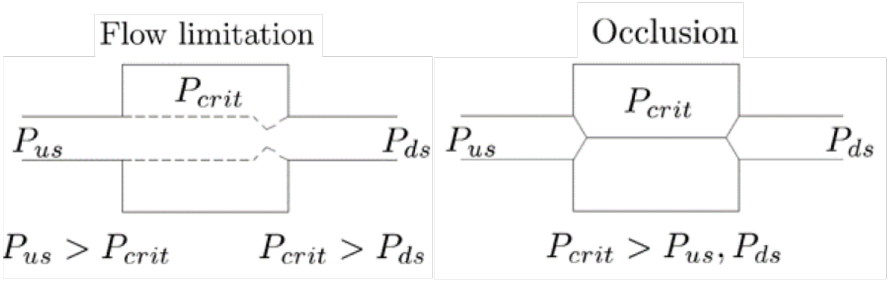

(a) **(b)**

Figure 1.1: (a) Flow Limitation, (b) Occlusion,

This setup will facilitate several parameter studies and a deeper investigation into the biomechanics of human upper airways, aiming to enhance our understanding of these dynamics and contribute valuable insights into respiratory health and disease mechanisms. Despite extensive efforts, there is still a lack of a robust two-way coupled, transient fluid-structure interaction (FSI) model that captures the critical physical effects from initial deformation to total occlusion of the airway model. Achieving such a model holds significant promise for predicting and diagnosing critical respiratory events like sleep apnea and lung wheezing.

1.3 Goals

This thesis aims to achieve several objectives: first, to identify a robust set of parameters for conducting FSI simulations under realistic physical conditions. Second, to conduct finite element method (FEM) simulations on a solid model of the Starling resistor. Third, to perform transient, implicit FSI simulations under various expiration pressure conditions. Additionally, the research will investigate the influence of hyperelastic material properties of human tissue. Finally, the study will analyze and identify the conditions leading to airway collapse and oscillation.

1.4 Limitations

The scope is limited to simulations using the latest release of Simcenter STAR-CCM+ and will utilize computational resources available at Chalmers. Due to time constraints, this study will not explore variations in human airway geometries. Instead, it will focus primarily on enhancing the model and investigating physical conditions within the constraints of the developed setup. While patient-specific applications are not within the immediate scope of this thesis, they could be considered for future research.

2
Theory

The following sections present the literature review for this master thesis.

2.1 Anatomy of the respiration system and lungs' sound terminology

2.1.1 Anatomy of the respiration system

The upper respiratory system begins with the connection of the nose and mouth to the trachea. At the back of the throat, the pharynx serves as the meeting point for the oral and nasal cavities. Extending downward from the pharynx, it connects with both the esophagus and the larynx. The larynx, which houses the vocal cords, signifies the shift to the lower respiratory system.

The trachea moves down and splits into the primary bronchi. These primary bronchi then divide into secondary (lobar) bronchi and later into tertiary (segmental) bronchi. The air passages continue to divide into bronchioles, which can be distinguished from bronchi by the lack of cartilage in their walls. This branching process ends in groups of alveoli. This system called the respiratory tree, consists of approximately 23 generations of branches and around 150 million human alveoli.

The intricate network of the pulmonary circulatory system extends throughout the lungs alongside the respiratory tree. This system differs from the respiratory tree as it is composed by two distinct systems—one of arteries and one of veins—interconnected by capillaries surrounding the alveoli. The arterial network usually mirrors the path of the respiratory tree, often running alongside bronchioles, whereas the venous network functions more autonomously.

The connection of the respiratory and circulatory systems is at the alveoli, which gather around alveolar ducts at the end of the respiratory tree. These dense clusters of alveoli result in ducts without distinct walls, forming a system that divides lung space into small sections. This arrangement, called the parenchyma or lung tissue, consists of capillaries and various tissues. The intricate network gives an excised lung a fragile, spongy, and elastic texture [20].

2.1.2 Lungs' sound terminology

For many years, doctors have been able to hear lung sounds and distinguish between healthy and unhealthy lungs. Thus, lung sound terminology is crucial for diagnosing diseases quickly and accurately. Recent reviews [21], [22] provide a comprehensive dictionary of terms, including several used for specific types of lung sounds. The terms were categorized as "continuous" and "intermittent" sound [23]. Previously, it was suggested that sounds be divided into tonal (wheezes) and non-tonal (crackles) sounds. Upon investigation, it becomes evident that the pairs "continuous" and "tonal" and "intermittent" and "non-tonal" are equivalent [1].

The previous study further support this, noting that correct use of lung sound terminology appears in only one-third of the papers they reviewed. This lack of consensus means that doctors cannot reliably distinguish these subtle variations in sounds, limiting the use of lung sounds for diagnoses.

2.2 Biofluid mechanics on collapsible tubes

Biological fluids display complex behaviors that are crucial to understanding physiological processes. Most biological fluids can be assumed to have constant density, allowing for the use of the incompressibility condition in Cartesian coordinates [7]. However, real flows in the body are often more complex than ideal Poiseuille flow due to the presence of bends, twists, and bifurcations commonly found in arteries and airways [7].

Biological vessels' shape has a big impact on flow patterns. The mean velocity profile is distorted and wall shear stress on the inner side of bends is decreased by secondary flows brought about by curvature and torsion [7]. Areas of low wall shear stress under stable conditions result from flow separation, which happens at abrupt contractions, expansions, and bifurcations. When Reynolds numbers are higher than 1, viscous boundary layers form, adjusting flow. These layers frequently expand to lengths greater than what is possible in straight segments of arteries or airways [7].

In fluid dynamics, especially in the airways, vessel flexibility is vital. Partial airway collapse during forced expiration can cause flow restriction; this is a condition that is made worse in those who are having asthma attacks [7]. The sound of wheezing is caused by self-excited oscillations of the walls of the airways. It is a noisy event similar to a flag flapping in the wind. Other sounds that can be heard, such crackles and snoring, are connected to liquid plug popping and obstructive sleep apnea, respectively [7].

Most vessels in the body maintain a higher internal pressure than external pressure, resulting in a nearly circular cross-section that minimizes flow resistance [8]. However, when subjected to significant negative internal pressure, these vessels can deform asymmetrically. In this state, the vessel's rigidity is primarily affected by its limited resistance to bending, leading to significant shape changes even with small

fluctuations in internal fluid pressure [8]. This creates a strong interaction between the fluid and the vessel's structure, potentially leading to self-excited oscillations. Examples of this phenomenon include wheezing during forced exhalation, Korotkoff sounds during blood pressure measurement, and cervical venous hum caused by oscillations of the external jugular vein [8].

It's important to note that in most physiological conditions, the fluid flows can be modeled as incompressible, with the highest Mach number being approximately 0.1 [24]. Additionally, air can be approximated as a Newtonian fluid in these contexts. These approximations allow for simplified yet accurate modeling of complex biological fluid dynamics.

Understanding these fluid-structure interactions is crucial for comprehending various physiological processes and pathological conditions. The interplay between fluid flow, vessel geometry, and structural properties of biological tissues continues to be an area of active research, with implications for both clinical practice and biomedical engineering.

2.3 Theory of FSI

Fluid-Structure Interaction (FSI) describes a subset of physics problems where an interplay between a fluid medium and a deformable structure takes place. Such interactions manifest themselves in a diverse range of engineering domains, including the fluttering of an airfoil (aeroelasticity), loads on stent-grafts from blood flow (biomechanics) and wind-induced oscillations of bridges (civil engineering).

However, this diversification comes at a cost; namely the insufficiency of an archetypical approach. Since each engineering problem carries its unique challenges, the method of solving such FSI problems is far from generic. Each problem to be solved relies on some degree of engineering assessment.

By understanding the theoretical background presented in the upcoming sections, we aspire to unravel the different approaches used in confronting real-world FSI problems. By then, the hope is that the reader will have gained a nuanced understanding of how such assessments are done in addition to grasping the preferred approach used in this paper.

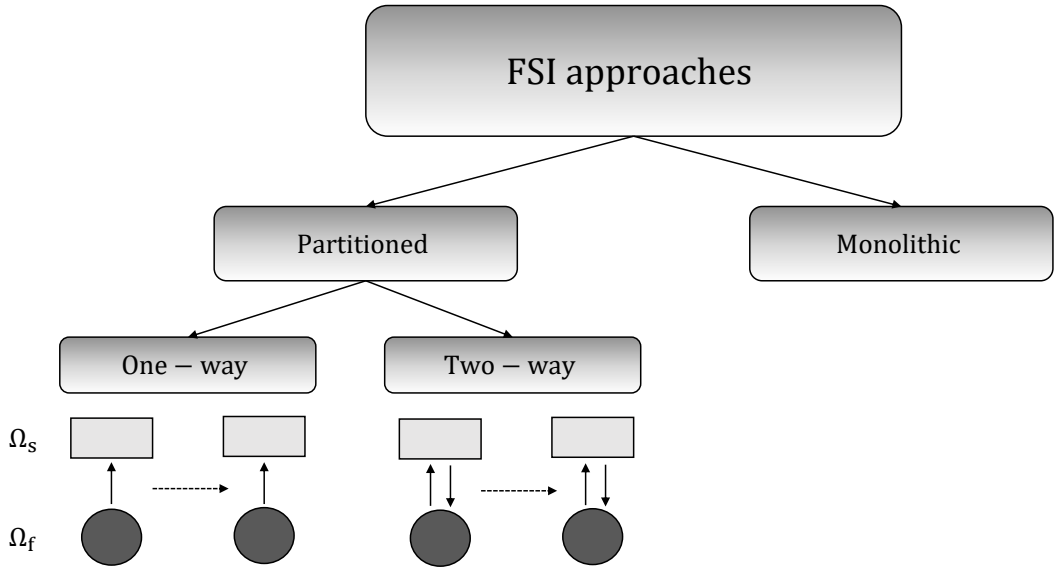

Figure 2.1: A schematic overview of the different FSI approaches that are presented in this section. Ω_s and Ω_f is the solver for the structural and fluid domains respectively. Horizontal dashed arrows represent jumps in iterations.

2.3.1 The monolithic and partitioned approach

When employing the monolithic approach, the structural and fluid parts of the problem are formulated together. This means that the governing equations for the structure and fluid at the interfaces where they interact are solved simultaneously. The upsides of using this method are accurate results with the requirement of a conformal mesh at the FSI interface. Choosing the monolithic approach for solving FSI problems also means that a distinctive solver has to be used, which is often not at hand for the diverse range of problems that FSI deals with [25][26].

For the partitioned approach, the structural and fluid systems are solved separately without the need to impose conformal meshes. Furthermore, two distinct solvers can be used that are specialized for each subproblem. As a consequence, the solution reaches higher rates of convergence issues. These challenges arise especially when dealing with strongly coupled cases [25][26].

2.3.2 One- and two-way coupling

Whether the problem is weakly or strongly coupled will also have consequences on the choice of approach. Weakly coupled FSI problems include problems where the flow imposes large deformations on the structure, but the reaction from the structural part upon the fluid is negligible. The converse claim is also considered weakly coupled. In such cases, it's sufficient that the information from one of the two solvers is exchanged in a unidirectional fashion and we can hence make use of

so-called one-way coupling. For instance, the fluid provides forces and pressures exerted on the structure, which the structural solver then uses for calculating the displacements without exchanging information back to the fluid solver. See one-way coupling in Figure 2.1. A simple example includes a flag during a windy day [26][27].

For strongly coupled FSI problems, the feedback from the structure (or fluid) can't be neglected. In this case, information has to be exchanged bidirectionally between the two solvers. As the structure deforms, the information is exchanged to the fluid solver that updates the geometry along with other relevant information, i.e. heating of the structure. See Figure 2.1.

It's important to note that the time steps don't necessarily have to match between the solvers in the partitioned approach. The time step is problem-specific, and also partly depends on how fast the deformations take place in the structural domain. For fast feedback, it might be compulsory to impose alike time steps for the distinct solvers to capture the interaction fully [26][27].

2.3.3 Challenges of FSI in collapsible tubes

Fluid-Structure Interaction (FSI) involving collapsible tubes presents several challenges. Firstly, it can be difficult for the solver to handle the fluid-solid interface, particularly in the case of collapsible tubes with significant solid deformations. To address this, frequent remeshing of the fluid domain may be necessary, as the new fluid domain and its deformation are not known, requiring interpolation between the old and new meshes [28].

If a partitioned solver is used, instabilities can arise from the unknown fluid boundary and mesh deformation, especially in large deformations [29]. This issue can be mitigated by employing under-relaxation factors for the data transfers, albeit at the cost of increased computational effort.

Another challenge is the potential occurrence of oscillations in collapsible tubes, which may be influenced by the time resolution used for numerical simulation [30]. Addressing this requires knowledge of the oscillation frequencies from experiments, allowing for the selection of an appropriate simulation time step. As a rule of thumb, using 1%-10% of the period of the Nyquist frequency of the oscillations' frequency is recommended.

It's important to note that the modelling of collapsible tubes often involves the use of non-linear, specifically hyperelastic, materials. These material non-linearities, combined with potential geometric non-linearities in models of the human upper airways, further add to the computational complexity.

2.4 Previous studies on collapsible tubes

Forgacs [17] proposed theories about the wheezing mechanism in relation to three different musical instruments: a flute, a clarinet or oboe, and a toy trumpet. He excluded the first two instruments for two main reasons. Firstly, for them to produce wheezing frequencies, they would have to be longer than the airway branches. Secondly, while wheezing produces the same frequencies at different air densities, these two instruments do not exhibit this behavior. Therefore, Forgacs suggested that the wheezing mechanism is likely similar to that of the toy trumpet due to the significant role of the tube walls in creating the wheezing sound. However, this theory remains vague.

Later, there have been different experimental methods to investigate the origins of wheezing sounds. Most used a Starling Resistor model, consisting of a tube passing through a sealed box with two rigid segments and a collapsible segment [1]. Grotberg and Davis proposed that wheezing sounds happen when a fluid passes through a flexible passage and causes flutter [19]. Gavriely et al. carried out a study using a Starling resistor model, which involved a pliable tube held between two inflexible tubes [18]. They explored the connection between the flow rate, upstream and downstream pressures, and the occurrence of self-generated oscillations. They noted a correlation between flow restriction and self-generated oscillations, consistent with earlier findings [31].

Although these studies offer strong evidence that wheezing is a result of the self-sustained vibration of the airways as air passes through them, they do not provide a comprehensive and quantitative understanding of the mechanism, particularly without taking into account the effects of axial pre-tension, which exists in the lung [32]. A quantitative model is being needed for better diagnosis. Thus, we must delve more deeply into the broader literature that seeks to elucidate self-sustained vibrations in flexible tubes.

2.4.1 Theoretical models

The complexity of theoretical models has increased over time, starting with 1-dimensional models and progressing to simulations of the Navier-Stokes equations combined with an elastic tube model. Jensen recently reviewed the modeling of the Starling resistor [33], while earlier work on 2-dimensional models was summarized by Pedley and Luo [34]. There is a considerable body of work examining a related 2-dimensional model of the Starling resistor. This includes linear stability analyses by [9],[10], [11], [35] and [12]. Additionally, numerical simulations of the entire system have been conducted by [13], [34], [14], and [15].

Various instabilities such as travelling wave flutter, Tollmien-Schlichting waves, and static divergence have been identified but are yet to be fully confirmed in a 3-dimensional system. The complexity of the 3-dimensional modeling has delayed its development. Some studies have analyzed the flows resulting from prescribed wall

motions, including work by Heil and Waters [36],[37] and Whittacker[38].

An interesting finding of this research is that self-excited oscillation occurs when the oscillation is about a non-axisymmetric mean configuration. These studies have also presented some evidence of the sloshing mechanism. Theoretical studies have reasonably succeeded in predicting the qualitative behavior of Starling resistors, but accurately forecasting quantitative details has proved challenging due to the system's complexity.

While some mechanisms have been proposed, experimental validation is still pending. Our focus is on establishing quantitative relationships between the tube's geometry and material properties and the conditions leading to oscillations.

2.4.2 Numerical models

The study of fluid flow through collapsible tubes is a complex field with important physiological process consequences. Researchers have used various numerical methods and experimental approaches to investigate this phenomenon, focusing on both two-dimensional and three-dimensional models.

In 2D studies, such as those conducted by Huang [39], the lattice Boltzmann method has been used to solve fluid flow problems, while the nonlinear dynamics of collapsible channel walls are modeled using the Bernoulli-Euler Beam theory. These studies have expanded the parameter space to include high Reynolds numbers, high structure-to-fluid mass ratios, and high external pressures.

Three-dimensional analyses, as presented by [40], have employed finite element methods to solve the Navier-Stokes equations coupled with large, nonlinear deformations of elastic walls. These studies with validated results for cross-sectional shapes of thick-walled tubes and have found issues such as ill-conditioning and locking behavior. The effects of wall thickness on flow patterns have also been examined, revealing different deformation patterns in thick-walled tubes that lead to changes in flow behavior.

Hazel [41] used a fully coupled finite-element method to study steady flow through thick elastic tubes. This study brought to light the significance of the Bernoulli effect, which leads to a more severe tube collapse as compared to situations in which it is not present. Additionally, a basic characteristic that have been observed in strongly collapsed tubes was the development of 'jets' like flows, which was leading to significant changes in axial velocity profiles..

Zhang's work [42] focused on the behavior of flexible tubes under external pressure, developing a technique called rotating spines to adjust the mesh for large deformations. This research identified multiple solutions for a range of Reynolds numbers and determined the stability characteristics of the system using the eigenvalue method.

A 2D Starling resistor model by Stewart [43] investigates laminar high-Reynolds-number flow through a finite-length planar channel with a partially elastic wall, using eigenfunction expansions and numerical simulations to examine global stability. The research reveals a transition from high-frequency 'sloshing' at high tension to 'slamming' motion at low tension, with hydrodynamic modes increasingly contributing to instability as tension decreases. This simple model demonstrates how fluid inertia and membrane curvature control slamming dynamics, providing insights into fluid-structure interactions in channels with flexible walls.

Also, remarkable was Akbar's research [44] that introduces a 3D computational model of fluid-structure interaction for steady-state flow in a collapsible tube. He has found that the deformation of the tube is more notable near the end of the flexible section, with the fluid flow velocity showing a jet-like profile in the most deformed region and downstream. He also examines the convergence and stability of data transfer, finding minimal differences when changing convergence criteria. Flows with higher Reynolds numbers are more likely to cause 3-lobe buckling, with significant deformations occurring near the downstream end. Additionally, his study has found low-pressure areas at the junction of the flexible and downstream rigid sections, which is consistent with previous findings by Hazel [41] and Huang [39]. Furthermore, he observes a reverse flow downstream of the most deformed part, in line with experimental results from [6] Bertram and Godbole.

Recent work by Laudato [45] examined the relationship between geometric characteristics of Starling resistors and contact critical pressure using a computationally validated model based on experimental data. He used a hyperelastic model, because large deformations occur at the tube. Also, he established a connection between contact critical pressure and the initiation of self-excited oscillations in collapsible tubes. His results demonstrated that increasing tube thickness and pre-stretch ratio, while decreasing the length-to-diameter ratio, leads to higher critical collapse pressures.

Furthermore Laudato [46] has conducted CFD LES models to investigate experimentally validated geometries of flexible tubes with a velocity inlet 10 m/s. This research focused on the acoustic properties of collapsible tubes, introducing the concept of an acoustic tube law. The results have shown that the highest sound power is generated in the post-buckling configuration, Also, he suggests that this results is important for understanding self-excited oscillations and wheezing sounds in the lungs. In addition his findings resemble those of [47] Kounanis and Mathioulakis, where they have found a jet that passes from the mid cross section of the tube, it remains attached to one surface due to the Coanda effect, while also encountering flow separation on the opposite surface, leading to a flow symmetry brake.

Finally, these studies have improved our understanding of fluid-structure interactions in collapsible tubes. They have shown us complex relationships between fluid flow, tube deformation, and acoustic properties, while also highlighting the importance

of factors such as Reynolds number, wall thickness, and external pressure. But so far none of them have developed an FSI unsteady-state model close to Gregory's Starling Resistor model, which closely resembles the human lungs and examines the frequencies of the self-exciting oscillations that Gregory has discovered [1].

2.4.3 Experimental models

2.4.3.1 Previous experimental models

Most of the experimental approaches have focused only on finding out instabilities by using water as the working fluid [6], [48], [49], [50]. However, the use of water in these studies limits their relevance to the lung, as the ratio of tube wall density to fluid density is off by three orders of magnitude. Additionally, the studies do not take into account the axial tension within the lung airways [32], which occurs during breathing. Also, while there have been numerous experimental studies conducted, the variations in specific setups make comparisons difficult.

Later, other experiments were conducted using air as a fluid by [7], [1], [51]. Their setup was similar to Gregory's, who used a Starling resistor model. This model will be explained in detail in the next subsection because this thesis goal is to replicate his experiment's results.

According to the above experiments the collapsible tube's two-lobed collapse produces two jet-like flow structures in the plane of the tube's major axis. These jets impact the tube wall near the downstream end of the collapsible segment, creating two sickle-shaped (and sometimes complete annular) areas of increased axial velocity before merging further downstream. A region of retrograde flow forms near the tube's centerline when the tube undergoes significant collapse. These flow characteristics are incredibly robust and have been observed across a wide range of Reynolds numbers, from laminar flows at Re $\approx$ 300 [52] to fully turbulent flows at Re $\approx$ 10,000 [53]. The oscillation frequency is relatively low.

However, experiments demonstrate that the most significant fluctuations in flow rate typically occur downstream of the collapsible segment, while the inflow rate remains nearly constant [52]. This suggests that the oscillations cannot be driven by the sloshing mechanism discussed above. For sufficiently thin-walled tubes, self-excited LU-type oscillations can occur at Reynolds numbers as low as $\approx$ 250, with a maximum frequency of about 10Hz. [54] noted that the oscillation frequency decreases as the length of the downstream rigid tube, Ldown, increases [55], while a change in Ldown does not impact the Reynolds number at which the oscillations initially develop.

It is worth to be mentioned that an investigation was conducted by [56] on the collapse of flexible tubes due to capillary pressure. The evolution of the tube's cross-section was documented by [57], who identified three distinct states of oscillation. Zayko and Vedeneev have shown that the magnitude of tube oscillation is greater in turbulent conditions compared to laminar conditions [58]. Yiasemides

observed asymmetrical flow separation downstream of the tube neck and suggested that this could act as a triggering mechanism for tube oscillations [59].

Also, Kumar studied the behavior of a collapsible tube under forced oscillations across different Reynolds numbers [51]. At low Reynolds numbers, the tube exhibits small-amplitude oscillations close to a collapsed state, transitioning to large-amplitude oscillations, and then small-amplitude oscillations as Reynolds number increases. Weak forcing can induce symmetric milking-mode-like oscillations at low Reynolds numbers and cause quasiperiodic or chaotic behavior at higher Reynolds numbers. The interaction between limit-cycle oscillations and periodic forcing leads to complex dynamics, including quasiperiodicity and chaos, which are not observed in unforced cases. The introduction of periodic forcing adds a dimension to the system's phase space, increasing the likelihood of chaotic behavior.

2.4.3.2 Gregory's experimental model

A recent study by [1] employed a Starling Resistor model to investigate fluid flow dynamics in flexible tubes. This model consists of a flexible tube flanked by two rigid tubes, all enclosed within a chamber where external pressure can be applied to the flexible segment.

Experimental Setup and Conditions: The experiment was conducted using air as the fluid medium, maintained at a constant body temperature of 37°C [60]. Atmospheric pressure was set at 101,325 Pa. The air was treated as a Newtonian fluid with uniform and isotropic properties. Considering variations in pressure, temperature, and humidity, the air's viscosity was estimated to range from 18.9 to 19.2 μPa s, while its density varied between 1.04 and 1.20 kg/m^3.

The flexible tube was designed to be isotropic and homogeneous, with material properties defined by Young's Modulus (E) and Poisson's Ratio (v). Based on previous studies [61], [62], [55], the Poisson's ratio was assumed to be between 0.45 and 0.49, typical for incompressible soft tissues. The Young's modulus was estimated to range from 0.1 to 2 MPa, acknowledging significant uncertainty in this parameter.

The geometry of the tubes was based on the Horsfield lung model for humans [63], which categorizes the human lung network into 35 different segment sizes. In the lung region where wheezing is believed to originate, the length-to-diameter (l/d) ratio falls within 1.3-4, and the thickness-to-diameter (h/d) ratio ranges from 0.03 to 0.2.

Experimental Procedure: Gregory controlled the external pressure, inlet and outlet pressures of the flexible tube, and the average flow rate Q. The experiment was conducted slowly to establish quasi-steady state solutions at each time point.

Initially, the flexible tube was open. As the downstream pressure decreased, the flow rate increased rapidly while the tube remained open. Further increases in suction led to a decrease in pressure inside the tube relative to its surroundings due to the

upstream rotameter.

The experiment revealed several key phases:

1. Tube collapse: At around 50 seconds, the flow rate Q leveled off, indicating the onset of tube collapse.

2. Oscillations: Oscillations began at approximately 60 seconds, visible in the spectrogram.

3. Multiple oscillation modes: As suction increased, the tube underwent three distinct modes of oscillation before completely collapsing at around 150 seconds.

4. Reopening: When suction was gradually reduced to zero, the three oscillation modes were observed in reverse order before the tube fully reopened at about 250 seconds.

This experiment provides valuable insights into the behavior of flexible tubes under varying pressure conditions, mimicking exhalation. The observed oscillations and collapse patterns contribute to our understanding of phenomena like wheezing. This experiment is the closest to finding the mechanism of wheezing so far. That's why it was selected to be reproduced as an FSI unsteady-state simulation for this Master's thesis.

2.4.4 Mechanisms of the self-exciting oscillations

It's crucial to detect the frequencies and understand the mechanism behind the oscillations of the human airways that produce wheezing. With this knowledge, doctors can diagnose and treat patients effectively [1]. This chapter discusses the literature's opinions and facts about the mechanism of oscillations in collapsible tubes.

During the oscillations, the tube experiences a collapse with two lobes [8]. This type of collapse is the most common form of biological flows in the airways [46]. The collapse creates two jet-like flow structures in the plane of the tube's major axis [8], [5]. This jet impinges on the tube wall near the downstream end of the collapsible tube, creating sickle-shaped regions of elevated axial velocity. The jet eventually merges further downstream. Also, a region of retrograde flow develops near the tube's center-line when the tube is sufficiently strongly collapsed [8], [5].

These flow features are described as robust and fundamental because they exist for a wide range of Reynolds numbers from 300 (Bertram et al. 2008) to 10,000 [53]. Also, the visualization of the flow downstream of the oscillating collapsible tube reveals secondary shear-layer instabilities that have a much higher frequency than the tube oscillations [52] and these can create different flow features downstream.

Ohba have shown a single, central jet downstream of the collapsible tube [64]. Also,

[47] and [59] have suggested with their experiments that the onset of self-excited oscillations may be associated with symmetry breaking of the flow downstream of the throat because they observed the Coanda effect. In their work,[47] and [59] observed a consistent decrease in internal fluid pressure from the inlet to the outlet. This decline is attributed to viscous effects, as well as the fact that high flow speeds through narrow stenosis result in low pressures [5]. The formation of a neck in the tube leads to a sudden constriction in area, converting the flow's kinetic energy into pressure energy, causing an increase in upstream pressure that exceeds the opposing chamber pressure, leading to the opening of the neck, resulting in the tube's oscillation [51].

Also, [46] has shown the Coanda effect in his results too. He conducted numerical simulations with low Mach velocities (0.12) on Starling resistor with stable geometry. He has shown that a jet attaches to one side of the domain and creates a recirculation region on the other side. According to him, the periodic flow separations cause an oscillating force perpendicular to the flow, turning the flow into a dipole source, resulting in the generation of sound from fluctuating forces due to flow separation. Furthermore, he explains that the collapsible tube acts as a compact acoustic source, with both aerodynamic and acoustic pressure fluctuations being observed. Acoustic waves are generated at the frequency of flow shear-layer fluctuations. Also he observed that short wavelength pressure features downstream have an aerodynamic origin, while larger wavelength pressure fluctuations move at the speed of sound, mostly upstream. According to him, acoustic waves are generated by fluid dynamics features like the broken symmetry, potentially playing a role in the onset of self-excited oscillations.

An important observation made by [34] is the presence of vorticity waves in their model. [39] mentions that these waves occur for $550 \leq \mathrm{Re} \leq 3000$. These waves grow downstream of the neck in a collapsed channel. The exact role of these vorticity waves in the development or persistence of self-excited oscillations in three-dimensional tubes is not yet clear. [51] suggests that both asymmetry and vorticity waves may play important roles in the onset or maintenance of self-excited oscillations.

This is because the generation and shedding of vortices play a major role in system stability, and these waves might create instabilities in wall motion due to shear layer instabilities [39]. [51] noticed that his tube was oscillating between two different buckle positions: one in the middle of the tube and the neck, and one closer to downstream. [39] also suggests that self-excited oscillations can be triggered by high external pressure and that the oscillating amplitude increases with Pe.

In Gregory's [1] experiment on a quasi-steady state, the oscillations began at a critical point where p1-pe levels off and starts to rise, and Q levels off and starts to fall, where p1 is the pressure at inlet and pe the external pressure. Initially, p1-pe and p2-pe were dropping while Q was increasing, where p2 is the pressure at outlet. According to Gregory's results, the oscillations start from the synchronization of

longitudinal waves with the opening and closing of the tube, suggesting the coupling of two oscillation modes causing instability, resulting from the interaction between the fluid and the tube.

In the experiment, the tube symmetrically collapses in the up-and downstream directions, with the narrowest point in the middle. He established a tube law characterizing the tube equilibrium without flow and a fluid law explaining the equilibrium of the fluid. The system is at equilibrium when the fluid and tube laws are equal. Gregory explains that oscillation onset occurs just before total collapse, in the buckling state where the stretching energy in the tube is dominant rather than the bending energy, which is dominant before the buckling state and at the post-contact state. He discovered that the collapse of the tube occurs around a 0.3 dynamic to collapse pressure ratio, allowing the estimation of the critical flow ratio for oscillations. Additionally, he notes that flow separation occurs at the onset of the oscillations downstream of the narrowest section.

The mechanism proposed for the self-excited oscillations is that eddies shed from the narrowest section, continue downstream and excite a longitudinal wave in the tube. The wave then reflects and travels upstream as an elastic wave, extracting energy from the flow if its frequency matches the tube's natural frequency. This occurs when there is flow separation and a pressure difference and the equilibrium between the tube law and fluid law, at the flow separation area of the fluid law.

Now it is crucial to discuss the concept of sloshing. According to Jensen [7], when the wall stiffness is high, small wall deflections can lead to high-frequency oscillations. These oscillations can cause periodic displacement of fluid from the collapsible tube into the rigid sections upstream and downstream. There is a net influx of kinetic energy into the system if the amplitude of "sloshing" flow is greater upstream than downstream. The oscillations extract energy from the mean flow, causing their amplitude to grow. The "sloshing" mechanism extracts energy more efficiently when the tube has a non-axisymmetric geometry, such as the buckling state [51].

Experiments have shown that self-excited oscillations can occur only on a non-axisymmetric geometry [37], [38], [52]. [65] confirmed through numerical simulations that self-excited oscillations occur due to the sloshing mechanism in initially axisymmetric elastic tubes and Whittaker [38]mentioned that the instability occurs due to the interaction between fluid and solid mechanics, rather than being caused by a hydrodynamic instability modified by the elastic tube wall.

In a study by Stewart [43], it was found that high-frequency sloshing is caused by wave reflections of static divergence and traveling-wave-flutter modes at junctions with rigid channel segments. Heil [8] notes that the wall tension of the tube is essential to the oscillations. A reduction in wall tension leads to a lower oscillation frequency and excites a convectively unstable traveling-wave-flutter mode. Further reduction in tension leads to wave-like flow features downstream due to hydrodynamic mode excitation.

At low frequencies, the oscillations transition from sloshing to reduced total viscous dissipation. In 3D tubes, the slight buckling results in minor volume changes, leading to weak axial oscillatory flow. The dominant oscillatory flow in 3D tubes occurs in the transverse direction of the tube cross-section. These findings suggest that sloshing is not the initiating mechanism for these oscillations. Another interesting fact is that the largest fluctuations in flow rate typically occur downstream of the collapsible tube, and the flow rate at the inflow remains approximately constant. This contradicts the idea of sloshing as the mechanism for the oscillations [8].

Additionally, there are other findings, worth to be mentioned. First, researchers found that the length of the tube impacts the development of oscillations. In long tubes, the oscillations eventually stabilize into a large-amplitude limit cycle. It was also discovered that increasing the length of the downstream section does not affect the critical Reynolds number. This implies that the initiation of oscillations is not influenced by the downstream geometry [8]. In the study conducted by [51], it was found that at low Reynolds numbers, the collapsible tube experiences symmetric oscillations due to external forcing. However, self-excited oscillations take over at higher Reynolds numbers (above 200). Both experiments and theory indicate that the system is not always stable and can transition to a chaotic state via either a quasiperiodic route or a period-doubling route. Kumar [51] also observed that the oscillation frequency of the tube is influenced by the frequency of the external force acting on it. When the force frequency is close to the system's natural frequency, the aperiodic response of the oscillations is completely suppressed. Finally, Zayko and Vedeneev found that the amplitude of tube oscillations is higher in turbulent flow regimes compared to laminar ones [58] . This suggests that turbulence intensifies the oscillatory behavior of the tube.

3
Methods

3.1 Mathematical models

3.1.1 Structural equations

3.1.1.1 Governing structural equations

Solid mechanics studies the displacement of a solid continuum under prescribed loads and constraints [66]. The fundamental laws that govern the mechanics of solids follow similar principles as the mechanics of fluids laws, which are the conservation of mass, linear momentum, angular momentum, and energy. In solid mechanics, it is more common to express the conservation laws using a lagrangian approach, where the observer follows the solid material as it moves through space and time. Conservation of mass, in the lagrangian approach, mass is always conserved. The mass that is contained in any deformed volume is the same mass that was originally contained in the undeformed volume:

$$\rho_0 V_0 = \rho V \tag{3.1}$$

where: ρ_0 is the initial density V_0 is the initial volume ρ is the current density V is the current volume. The density in the deformed configuration is:

$$\rho = \rho_0 \frac{V_0}{V} \tag{3.2}$$

In conservation of momentum, the motion of a solid body is governed by Cauchy's equilibrium equation, which expresses the conservation of linear momentum for a continuum. In the Lagrangian approach, the convective term vanishes and the time derivative of the velocity reduces to the partial second derivative of the displacement:

$$\frac{\partial^2 u}{\partial t^2} = \nabla \sigma + b \tag{3.3}$$

where: u is the displacement of the solid body b is the total body force per unit volume σ is the Cauchy stress tensor

3.1.1.2 Hyperelastic materials

Hyperelastic material models characterize how materials can experience large elastic deformations when subjected to loads and return to their initial shape after the load is removed. In the case of hyperelastic materials like rubber, the relationship

between strain and stress is not linear.

The strain energy potential, W, defines the strain-stress relationship for hyperelastic materials: W = W(F)
The general strain-stress relationship can be expressed as:

$$S = 2\frac{\partial W}{\partial C} \tag{3.4}$$

, where C represents the right Cauchy-Green deformation tensor. This tensor characterizes the deformation of a material by relating the change in length of material line elements due to deformation.
For incompressible materials, the strain energy potential is split into deviatoric and volumetric parts:

$$W = W_dev + W_vol \tag{3.5}$$

With shear modulus and bulk modulus:

$$\mu = \frac{E}{2(1+\nu)} \tag{3.6}$$

and

$$K = \frac{E}{3(1-2\nu)} \tag{3.7}$$

.
The Neo-Hookean model's strain energy potential W is given by:

$$W = (\frac{\mu}{2})(I1-3) + (\frac{\kappa}{2})(J-1)^2 \tag{3.8}$$

The Ogden material model is typically used for materials with larger strains. The Ogden model's strain energy potential W is given by:

$$W = \Sigma(\frac{\mu_p}{\alpha_p})(\lambda_1^{\alpha_p} + \lambda_2^{\alpha_p} + \lambda_3^{\alpha_p} - 3) + (\frac{\kappa}{2})(J-1)^2 \tag{3.9}$$

, where the strain potential is written in terms of the principal stretches λ_1, λ_2 and λ_3, which are the eigenvalues of the modified right stretch tensor Specifically, for a single-term Ogden model, the initial shear modulus μ should be approximately equal to μ_1. For a more general Ogden model with multiple terms, the relationship becomes:

$$\mu = \Sigma_i(\frac{\mu_i * \alpha_i}{2}) \tag{3.10}$$

, [67].

3.1.2 Governing fluid equations

The fluid flow is unsteady and governed by the Navier-Stokes equations. Assuming the fluid is incompressible and Newtonian, the continuity equation is:

$$\frac{\partial u_i}{\partial x_i} = 0 \tag{3.11}$$

, (i = 1, 2, 3)
The components of the flow velocity are denoted by u_i. In the case of a fluid with constant density and viscosity, the momentum equations are formulated as follows:

$$\rho(\frac{\partial u_i}{\partial t} + u_j \frac{\partial u_i}{\partial x_j}) = -\frac{\partial p}{\partial x_i} + \frac{\mu \partial^2 u_i}{\partial x_j \partial x_j} + f_i \tag{3.12}$$

,i=1,2,3 where f_i denotes the body forces per unit volume acting on the fluid, ρ is the fluid density, p is the pressure, μ is the dynamic viscosity, and t is the time. The term on the left-hand side represents the unsteady convection term, while the second term on the right-hand side is the diffusion term [66].

The no-slip boundary condition at the stationary walls is given by:

$$u_{i,wall} = 0 \tag{3.13}$$

3.1.3 Governing FSI equations

At the Fluid-Structure Interaction (FSI) interface, the behavior of the fluid and solid must satisfy both kinematic and dynamic criteria to ensure accurate coupling between the two domains [68], [69].

The kinematic criterion ensures that the motion of the fluid and the solid is continuous across the interface, preventing any separation or penetration. This is also known as the geometric continuity where the fluid and solid must maintain contact without gaps or overlaps. This is expressed mathematically as:

$$d_{fluid} = d_{solid} \tag{3.14}$$

Here, d_{fluid} and d_{solid} represent the displacements of the fluid and solid respectively, and Γ denotes the interface surface.

Secondly, the dynamic criterion guarantees that the forces exerted by the fluid on the solid and vice versa are balanced. This is a condition of force balance,where the forces exerted by the fluid and solid on each other must be equal and opposite. This is represented as:

$$\sigma_{fluid} * n = \sigma_{solid} * n \tag{3.15}$$

Where σ_{fluid} and σ_{solid} are the stress tensors in the fluid and solid, and n is the unit normal vector to the interface Γ.

In many fluid-structure interaction (FSI) problems, a third condition is often included: the no-slip condition. This would require the fluid velocity at the wall to match the rate of solid displacement at the interface. For an unsteady state simulation, a third condition is necessary at the fluid-solid interface. This condition ensures continuity of velocity and is often referred to as the velocity kinematic condition or no-slip condition. It can be written as:

$$v_{fluid} = v_{solid} \tag{3.16}$$

Where v_{fluid} is the fluid velocity and v_{solid} is the velocity of the solid boundary at the interface on Γ. In terms of displacements, this condition can also be expressed as:

$$\frac{\vartheta d_{fluid}}{\vartheta t} = \frac{\vartheta d_{solid}}{\vartheta t} \tag{3.17}$$

This condition ensures that there is no relative motion between the fluid and the solid at their interface. It effectively means that the fluid "sticks" to the solid boundary and moves with it.

These conditions ensure a physically consistent coupling between the fluid and solid domains in the FSI problem, maintaining both geometric and dynamic continuity across the interface.

3.2 Numerical models

3.2.1 Structural equations

For compressible materials, the governing equations have only one unknown, which is the displacement field [70]. However, for materials that are nearly incompressible, Simcenter STAR-CCM+ employs a two-field method that uses two separate variables: the displacement field u and the pressure p. When dealing with large deformations, the internal forces become nonlinear relative to the displacements, so Simcenter STAR-CCM+ uses Newton iterations to solve the governing equations:

$$K_M^i \Delta u_N^i = r_M^i \tag{3.18}$$

where r_M^i are the residual forces at node M.
For the dynamics of a problem, the dynamic solution seeks the displacement field that satisfies the equation:

$$M_{MN}\ddot{u}_N + C_{MN}\dot{u}_N = f_M^{ext} - f_M^{int} \tag{3.19}$$

where M_{MN} and C_{MN} are the mass and damping matrices. The residual forces are then:

$$r_M = -M_{MN}\ddot{u}_N - C_{MN}\dot{u}_N - f_M^{int} + f_M^{ext} \tag{3.20}$$

Simcenter STAR-CCM+ offers two different methods for approximating accelerations and velocities, but only the First Order Backward Euler Method produced meaningful results. Therefore, this method will be detailed. It estimates the acceleration and velocity at the n-th time-step as follows:

$$\ddot{u}_N^n = \frac{\dot{u}_N^n - \dot{u}_N^{n-1}}{\Delta t} \tag{3.21}$$

and

$$\dot{u}_N^n = \frac{u_N^n - u_N^{n-1}}{\Delta t} \tag{3.22}$$

This first-order approximation is generally not recommended for high-resolution structural dynamics simulations because it can cause significant numerical damping.

However, this damping can be beneficial in eliminating unwanted initial transients or when the objective is to achieve a quasi-static solution.

Controlling the load stepping is also crucial. For scenarios involving nonlinear geometry (e.g. large strains and displacement) and nonlinear material properties (such as plasticity or hyperelasticity), the governing equations may become highly nonlinear, which can lead to divergence in the solution. To reduce this nonlinearity and enhance convergence, it is advantageous to apply external loads gradually over multiple steps.

Considering the static nonlinear problem:

$$r(u) = f_{int} - f_{ext} = 0 \tag{3.23}$$

With load stepping can be written as:

$$r(u^s) = f_{int} - \lambda^s f_{ext} = 0 \tag{3.24}$$

The stepping factor λ^s is used to control the incremental ramping of the load over the step s. Presently, Simcenter STAR-CCM+ implements a load loop strategy, where the external load is divided into segments that are applied incrementally over several load steps. In each of these steps, the nonlinear system, represented by Equation 3.24, is solved using the Newton-Raphson method:

$$u^s_{k+1} = u^{s-1} + \Delta u^s_{k+1} \tag{3.25}$$

$$\Delta u^s_{k+1} = \Delta u^s_k + du \tag{3.26}$$

and

$$r(u^s_{k+1} = f_{int}(u^s_{k+1}) - \lambda^s f_{ext} = 0 \tag{3.27}$$

3.2.2 Fluid equations

The model that has been selected on these simulations is the segregated flow method [71]. This solver solves the integral conservation equations for mass and momentum in a step by step sequence. When the governing equations are not linear, each one of them is being solved iteratively for the solution variables u, v, w and p.

This solver uses a pressure-velocity coupling algorithm to ensure that the velocity field complies to the mass conservation constraint by solving a pressure-correction equation. This equation is formulated from the continuity and momentum equations to generate a predicted velocity field that satisfies the continuity equation by adjusting the pressure accordingly. This approach is being called predictor-corrector method. The pressure variable is derived directly from the pressure-correction equation.

Originating from constant-density flow problems, the segregated solver is also capable of managing mildly compressible flows and low Rayleigh number natural convection. However, it is not appropriate for scenarios requiring shock-capturing, high

Mach numbers, or high Rayleigh number applications.

Some crucial aspects of the solver are covered below:
Firstly, is the discretization of the momentum equation. The momentum equation, for velocity = u, is

$$\frac{\partial(\rho \mathbf{u})}{\partial t} + \nabla \cdot (\rho \mathbf{u}\mathbf{u}) = -\nabla p + \nabla \cdot \tau + \mathbf{S_u} \tag{3.28}$$

,where ρ is the fluid density, u is the velocity vector, t is time, p is the pressure τ is the stress tensor and S_u represents source terms. The discretized form is

$$\frac{\partial(\rho \nu V)_0}{\partial t} + \sum_f [\rho \nu \nu a]_f = -\sum_f (\rho I a)_f + \sum_f T a \tag{3.29}$$

Next important part is the correction of the pressure. The pressure-velocity coupling is achieved by re-writing the continuity equation in terms of a mass flux correction $\dot{m}_f^{'}$:

$$\sum_f \dot{m}_f = \sum_f (\dot{m}_f^* + \dot{m}_f^{'}) = 0 \tag{3.30}$$

The $\dot{m}_f^*$ is the uncorrected face mass flux and is being calculated after the solving of the discrete momentum equations. For the solving of the momentum equations, the guessed pressure field p^* is being used, and it doesn't satisfies the continuity. For that reason the corrected mass flow $\dot{m}_f^{'}$ is being used, for the satisfaction of the continuity.

The discrete pressure correction equation is

$$p_p^{'} + \sum_n a_n p_n^{'} = r \tag{3.31}$$

,where the residual r is the net mass flow into the cell

$$r = -\sum_n \dot{m}_f^* \tag{3.32}$$

Simcenter STAR-CCM+ can execute the following pressure-velocity coupling algorithms SIMPLE, SIMPLEC and PISO.

On these simulations the SIMPLE algorithm has been used. This algorithm follows these 12 steps.

1. Set the boundary conditions.
2. Compute the reconstruction gradients of velocity and pressure.
3. Compute the velocity and pressure gradients.
4. Solve the discretized momentum equation. This creates the intermediate velocity field ν^*
5. Compute the uncorrected mass fluxes at faces $\dot{m}_f^*$
6. Solve the pressure correction equation. This produces cell values for the pressure correction $p^{'}$.

7. Update the pressure field:
$$p^{n+1} = p^n + \omega p^{'} \tag{3.33}$$
where ω is the under-relaxation factor for pressure.
8. Update the boundary pressure corrections $p_b^{'}$.
9. Correct the face mass fluxes:
$$\dot{m}_f^{n+1} = \dot{m}_f^* + \dot{m}_f^{'} \tag{3.34}$$
10. Correct the cell velocities:
$$\nu_p^{n+1} = \nu_p^* - \frac{V \nabla p^{'}}{a_p^u} \tag{3.35}$$
where $\nabla p^{'}$ is the gradient of pressure corrections, a_p^u is the vector of central coefficients for the discretized velocity equation, and V is the cell volume.
11. Update density due to pressure changes.
12. Free all temporary storage.

3.2.3 FSI coupling algorithm

Simcenter STAR-CCM+ offers a concurrent solution approach for addressing fluid-structure interaction (FSI) issues involving deformable solids [72].

First, the method of coupling between the fluid and the solid must be determined. The motion can be defined as either rigid or solid displacement, with both options allowing for either an uncoupled or fluid load specification as traction. For the FSI simulations in this thesis, a two-way data transfer approach has been chosen, where data is exchanged bidirectionally between the fluid and the solid. More specifically the fluid load pressure and wall shear stress.

The fluid traction is transferred from the fluid side to the solid side, where it is applied as a load. To minimize information loss during interpolation, it is recommended to use a similar mesh resolution on both sides of the interface. The interpolation scheme accommodates both conformal and non-conformal interfaces.

Also, The information transferred from the solid to the fluid is the interface deformation. This solid displacement is automatically interpolated from the solid side of the interface to the fluid side. To prevent loss of information during interpolation, it is advisable to use a similar mesh resolution on both sides of the interface. The interpolation process supports both conformal and non-conformal interfaces.

To apply these interpolated displacements, Simcenter STAR-CCM+ adjusts the mesh on both sides of the interface. The mesh in the solid region is deformed using the Solid Displacement motion, while the mesh in the fluid region is adjusted with the Morpher motion.

Finally, one of the most important thing on an FSI simulation is the solution stabilization. Simcenter STAR-CCM+ provides two stabilization methods for solutions: Dynamic and Constant Displacement Under-relaxation.

The Dynamic method aims to enhance the performance of FSI simulations by anticipating the fluid tractions that arise from changes in the interface position. It operates under the assumption that a specific volume of fluid moves along with the FSI boundary, effectively acting as an added mass. This method is particularly recommended for two-way coupled problems.

3.3 Simulation setup

3.3.1 Solid cases

The geometries that have been used, derived from Gregory's flexible tubes that he used for his experiments. According to the thesis developed by Gregory, 11 tubes were used. The primary dimensions of these tubes include initial length (L0), length after the axial pre-stretch of the tube (L), thickness of tube (h) and radius of the tube (a). Typical values of these properties are L0=18.9mm - 22.4mm, L=19.2mm-28mm, h= 0.19mm-0.38mm and a=3.15mm-3.4mm. In addition, Laudato applies elliptical tubes. Specifically, in order to manipulate the buckling direction and achieve a two-lobed buckling pattern, the tube has an elliptical radial cross section with the minor axis aligned vertically and a length of 0.99r.

Table 3.1 shows the solid's case characteristics. In this simulation, a rubber-like material has been used to solve big deformations of the tube. Due to the large deformations involved, a linear elastic material is not suitable. Therefore, hyperelastic models are being used, specifically New-Hookean model capturing the nonlinear stress-strain relationship typical of rubber-like materials. Especially, New-Hookean model fits for rubber materials, that's why have been chosen in our case too. The material is treated as nearly incompressible, with a Poisson's ratio of 0.49 and Young Modulus 1 MPa, and density $1100 kg/m^3$. Also, the shear modulus and bulk modulus have been calculated according to equations 3.6 and 3.7.

Tube Geometries	Elliptical 0.99R
Material	Rubber
Hyperelastic Model	New-Hookean
Young Modulus	1MPa
Poisson's Ratio	0.49
Density	1100 kg/m3
Solver	Implicit Unsteady – First Order
Simulation Time	30 seconds
Installation Time	15 seconds
Adapted Time Step	0.001 – 1 seconds
Simulation Real Time	15 minutes

Table 3.1: Solid case characteristics

According to Laudato's mesh sensitivity analysis [45], the best option for the tube mesh was chosen. The geometry mesh was being created by using a directed mesh with 64 angular elements and 100 longitudinal elements.The mesh can be seen at figures 3.1 and 3.2. For temporal discretization, implicit unsteady solving with an adaptive time step method is used to facilitate efficient and detailed computation of time-dependent phenomena such as buckling of the tube.

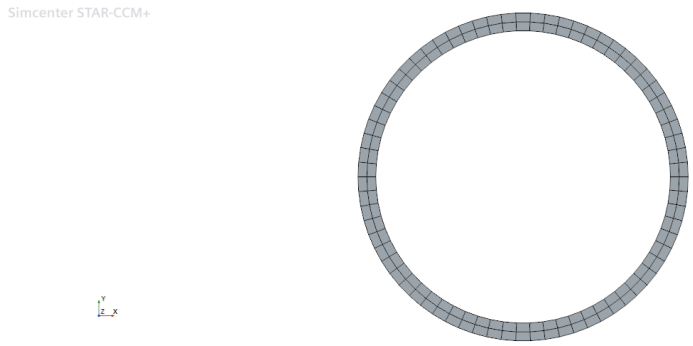

Figure 3.1: Angular elements

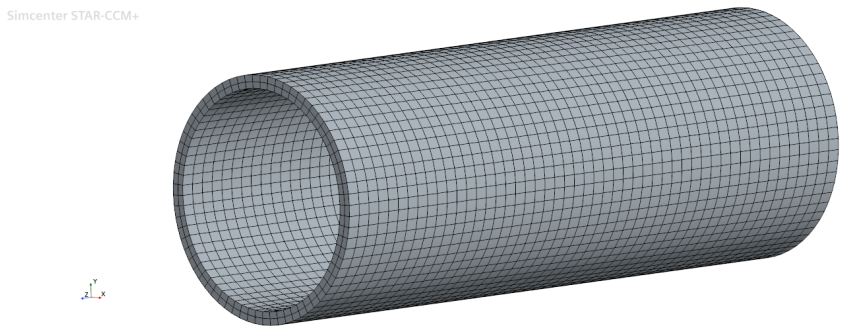

Figure 3.2: Longitudinal elements

At the contact phase of the tube, a critical consideration is preventing element interpenetration between opposing sides of the tube walls as they deform. To solve this,

a very thin plate has been placed strategically at the center of the tube. This plate serves as a contact surface that prevents unrealistic deformation behavior. Interactions between tube walls and central plates are modeled using a penalty method with frictionless contact. In addition, when deforming walls of the tube reach this centered plate, it is subjected to an applied small but significant force 3.33E9 Pa which acts perpendicularly to them and in opposite directions to external pressure.

Furthermore, the simulation includes the pre-stretching conditions observed in Gregory's experiments [1]. The inlet side of the tube is modeled with fixed constraints, preventing any movement. On the contrary, the outlet side of the tube is subjected to a stretching force, with the amplitude calibrated to match the values reported in Gregory's studies. The formula for the strain ramp is

$$\frac{\text{Strain Amplitude}}{\text{Final Installation Time}} * \text{Time} \tag{3.36}$$

Now the last segment for the simulation is the pressured surface which is the external surface of the tube. For the modeling of this, pressure has been used as solid stress load, also the surface load linearization was activated and the formula for the pressure ramp is

$$(\text{Initial Pressure} + \frac{\text{Pressure Amplitude - Initial Pressure}}{\text{End Time - Initial Pressure Time}} * (\text{Time} - \text{Initial Pressure Time}) \tag{3.37}$$

Additionally, a symmetry segment has been implemented where the displacement of the tube walls in the y-direction is constrained to zero. This constraint is crucial in promoting the formation of a two-lobe buckling pattern during the simulation.

For these solid case studies, 8 tubes have been selected from Gregory's database, including 3 that match Laudato's choices for better validation [45], [1]. All of the tubes are following Laudato's technique of elliptical tubes to achieve two lobes buckling [45]. The 3.2 below outlines their dimensions. We chose these tubes strategically to explore how different parameters—such as pre-stretch amplitude, thickness, and radius—affect the FEM analysis and data accuracy. This wide range of choices helps to see which tube setups give the most accurate outcomes, giving important information about how well our model works in different situations.

The simulation runs for a total of 30 seconds, with the first 15 seconds dedicated to an initial installation phase where the pre-stretch of the tube takes place. At the 15th second pressure is started to be applied, ramping up from 0 Pa to a maximum amplitude of 6000 Pa. The time step is allowed to vary between 0.001 and 1 second, providing a balance between computational efficiency and accuracy in capturing rapid changes in the system's state. These values of the time step have been selected according to Laudato's sensitivity analysis, where the largest value of the acting pressure has to be 400 Pa/s to capture the tube's behavior at the buckling and contact phase [45]. For all the simulations 6 cores have been used and the duration of the simulation was approximately 15 minutes.

Tube Number	l	l0	h	a	Units
1	19.2374	18.9826	0.38	3.15	mm
2	21.1484	18.9826	0.38	3.15	mm
3	23.0594	18.9826	0.38	3.15	mm
4	24.3334	18.9826	0.38	3.15	mm
5	24.3334	22.4224	0.19	3.4	mm
7	28.1554	22.4224	0.19	3.4	mm
8	16.6894	15.1606	0.38	3.15	mm
11	22.4224	15.1606	0.38	3.15	mm

Table 3.2: Geometrical parameters of the tubes

Three goals were aimed for with the solid cases. Firstly, the confirmation that simulation's results were correct. To do this, a MATLAB code has been made that used data from the simulation to create Gregory's tube law and compared the curve from the simulation with the curve from real experiments [1]. The simulation data were derived from a table that charts 30 unique points distributed along the arc of the inner walls in the central region of the tube for each discrete time step. Secondly, it was important to look how much the tube needed to be shaped like an ellipse to cause a specific type of buckling with two lobes, based on its characteristics. For some tubes, the smaller radius should become even smaller, to values like 0.98r, 0.94r, and 0.9r. Lastly, an extra option of Star-CCM+ has been used, with the name mid side vertex, which is an additional node placed in the middle of an edge in finite element mesh with linear interpolation. Generally, this technique can represent more accurately complex geometries and capture better stress gradients.

3.3.2 FSI cases

This subsection is going to analyse the methods that have been used to achieve a stable FSI case with accurate results, which is the main goal of this thesis.

3.3.2.1 FSI case without pressure gradient

After the completion of the solid cases, the next step is to create an FSI case. For simplicity, the first case that has been created was an FSI based on the solid case without fluid pressure. The only force that was acting at the system was the external pressure to the walls of the tube. In this situation, it was simpler and quicker to see if the FSI case was similar to the solid case and matched Gregory's experimental results.

To create this FSI case, as said before, the solid case has been used as a base model. So the mesh of the tube is exactly the same with the solid case, with 64 angular elements and 100 longitudinal elements.

The next step was to create the fluid domain and to achieve that, the following procedure has been followed:

1. For the first step to create the fluid domain, the "Vector Warp" option in Star-CCM+ was utilized. This option allows specifying the vector field function upon which the warp surface is based. The vector field used in this case was "normal", which provides information about the normal vector of a surface. The entire tube was selected as the geometry part, allowing the deformation of the tube to be recorded at every time step.
2. Based on the vector warp tube, the fluid domain inside the tube was created using the "fill holes" and "extract volume" commands.
3. The fluid domain inside the tube was then extended upstream and downstream. The distances for the upstream and downstream extensions matched Gregory's experiment, being 88 mm and 47 mm, respectively.
4. The mesh for the entire fluid domain was created using the "automated mesh" command in Star-CCM+. The meshing method used for the surface of the fluid was "triangular", as it is both fast and accurate in complex geometries.
5. The base size of the mesh elements was selected to be 1×10^{-4} m, closely matching the mesh elements of the tube, while the minimum element size was set to 1×10^{-5} m.
6. Two "prism layers" were added to simulate the boundary layer at the interior tube walls.
7. For the volume mesh, the "polyhedral mesher" was chosen. Initially, a volume mesh of tetrahedral elements was created, which was then converted into polyhedral-shaped cells. The mesh for both the upstream and downstream sections was developed similarly.
8. The total number of cells was as follows:
   (a) - Tube: 6,400 cells
   (b) - Fluid inside the tube: 270,737 cells
   (c) - Upstream: 204,100 cells
   (d) - Downstream: 204,350 cells
9. The resulting mesh can be seen in Figures 3.3, 3.4, 3.5, and 3.6.

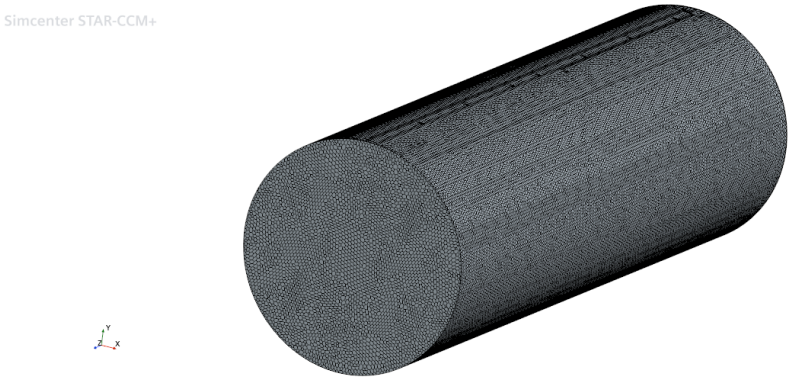

Figure 3.3: Fluid domain mesh

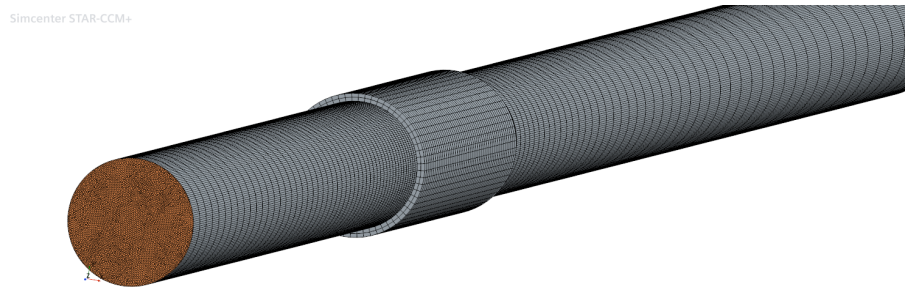

Figure 3.4: Mesh of fluid and tube

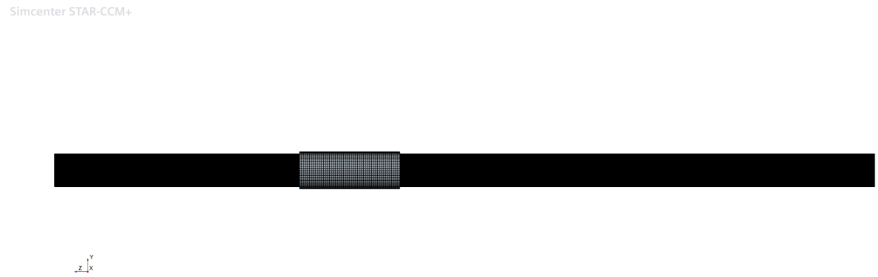

Figure 3.5: Mesh of the whole geometry

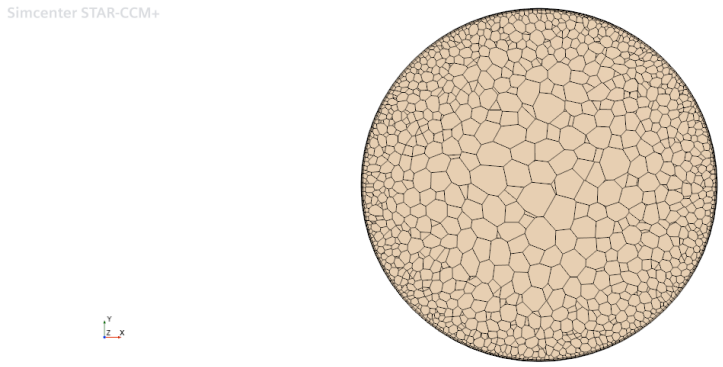

Figure 3.6: Mesh of fluid, perpendicular of z axis

Generally, in the FSI cases, only the "tube 2" was selected because its simulation tube law curve closely matched the experimental tube law curve in the solid case. Only one tube was chosen due to the time-consuming nature of FSI simulations, which can take anywhere from 2 to 7 days depending on the time step. Another difference with the solid cases is that now the tube law is being calculated in Star-CCM+ directly.

The same solid continua that were used in the solid cases were also applied to the solid part of the FSI case. For the fluid part, that its characteristics can be seen on table 3.3, the air has been used as a gas and the ideal gas model to express the density as a function of temperature and pressure and simplify the calculations of

the simulation. The implicit unsteady scheme was also applied like the solid continua. A laminar flow model was employed to keep the problem simplified. Also, the segregated flow model has been selected. The segregated solver utilizes a pressure-velocity coupling method to ensure mass conservation in the velocity field. This is accomplished by solving a pressure-correction equation derived from both continuity and momentum equations. The process involves predicting a velocity field that satisfies continuity, then adjusting the pressure to achieve this. This technique is often referred to as a predictor-corrector approach. The pressure variable is determined through the pressure-correction equation. The SIMPLE algorithm manages the solution update process in Star-CCM+. The segregated flow model has been chosen to be isothermal, which means that keeps the temperature in the continuum constant, to make the calculations faster.

Gas	Air
Gas Law	Ideal Gas
Flow Type	Laminar
Model	Segregated Flow
Solver	Implicit Unsteady – First Order and Morphing
Remeshing	Manually

Table 3.3: Fluid part characteristics

Also, the morpher solver have been used [73]. The boundaries of a region can change position and shape over time, so the morphing algorithm redistributes the mesh vertices in response to the displacement of the boundaries, allowing for non-rigid deformations of the mesh. The algorithm doesn't act on cell volumes, faces and edges. The initial movement that the morpher imposes on the mesh is defined though a set of control points. These control points originate from the mesh vertices on the morphing boundary, or from a control point table. Each control point is associated with a known displacement vector. The morpher uses these displacements to construct an interpolation field, which is used to calculate the displacements of all mesh vertices. The morpher uses the control point displacements to generate an interpolation field for the region, by which the morpher motion is defined. The morpher then uses the interpolation field to translate the mesh vertices to their new positions.

In our simulations, the BSpline interpolation algorithm is used. This method uses a hierarchical approach, progressively refining the control-point grid until the residual error falls within the specified tolerance limits. The process involves applying a series of corrections at various grid scales. To simplify, let xi, represent the coordinates at the i-th grid refinement step and t denote the target coordinates, with the residual being the difference $ri = t - xi$.

This residual, or displacement, is known at the control points but not elsewhere. The residual can be expressed as the sum of the interpolation Ii and the remaining residual ri-1 = Ii + ri until the desired displacement is achieved. An equation is

formed as:

$$t = x0 + \sum Ii + rn \tag{3.38}$$

where x0 represents the initial coordinates of the point, Ii denotes the interpolation at step i, and n is the final refinement step where the desired displacement is achieved. The refinement process continues until the morphing error converges within the specified morpher tolerance. The convergence of this algorithm is assured because, as the proximity data sets become smaller with each refinement level, they eventually contain only one control point, enabling exact interpolation to be achieved.

For this FSI setup, remeshing was considered a crucial setting. As said before, vector warp can record the deformation of the tube, and because of the strategy that has been followed to create the fluid domain, now it is possible to record the deformation of the fluid mesh elements too. So every time that the deformation of the fluid elements was big, and the quality of these elements was low, these elements could be remeshed manually, by executing all the mesh operations. On that way the simulation could continue to larger deformations of the fluid without having negative volumes. Figure 3.7 show the before and after of the remesh.

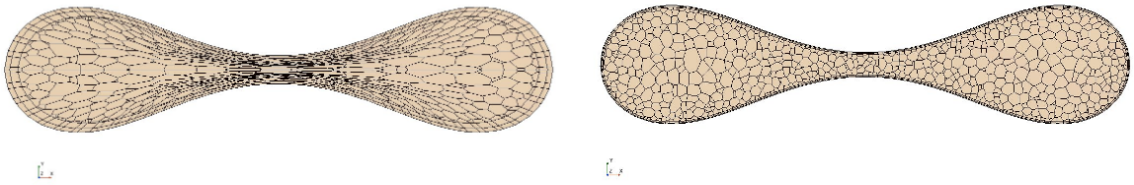

(a) **(b)**

Figure 3.7: (a) Fluid domain before remesh, (b) Fluid domain after remesh

It is important to mention that in FSI cases the elliptical geometries that Laudato used [45], didn't achieve their goal, to create a two lobes buckling. In order to achieve this specific buckling, a perturbation force has been used. The equation of the force is

$$P_{pert} = (1 - \frac{Time - InitialPressureTime}{EndTime - InitialPressureTime} * (A - Bx^2) \tag{3.39}$$

where the x is the direction x of the system and the perturbation constants are defined in accordance to (Lukas)

$$A = \frac{PressureAmplitude}{10} \tag{3.40}$$

and

$$B = \frac{A}{(a+h)^2} \tag{3.41}$$

, where the a is the radius and h the thickness of the tube.

So on the FSI cases the total pressure that acts on the external walls of the tube is equal to the subtract of the external pressure and the perturbation pressure.

$$P_{total} = P_{external} + P_{pert} \tag{3.42}$$

As the external pressure increases, the disturbance pressure decreases and should only be effective at the beginning to trigger the two-lobe buckling. This occurs because, according to the equations, the Ppert is greater for smaller values of x compared to larger values of x. So at the start, the total force that acts in the middle of the tube is bigger than the one that acts at the sides of the tube.

The boundaries of the tube in the FSI case are the same as those in the solid case. The only difference now is that the force acting on the tube surface is Ptotal from equation 3.42. For the fluid domain, all the tube walls in the experiment were defined as walls. The upstream inlet was defined as the pressure inlet, while the downstream outlet was defined as the pressure outlet. On this case the pressure difference between inlet and outlet was set as zero. All internal surfaces connecting the tube with the upstream and downstream sections were designated as internal interfaces. During the first 10 seconds of the simulation initialization, the tube is stretched as described in the solid section. The same stretching process applies to the downstream surface of the flexible tube, the fluid domain inside the flexible tube, and the downstream rigid tube. Additionally, in the FSI case, there is a mapped contact boundary where the fluid domain contacts the solid domain (flexible tube). The topology is indirect, meaning the mesh is not conformal across the interface, so there is no one-to-one correspondence between faces and vertices on the solid and fluid sides.

Finally, for the FSI simulation the end time was set as 25 second while the initial time was 10 seconds. For the simulations without fluid pressure the time step was 0.1 - 1 second. The simulation had an adapted time step system, where the control method that was used had the name target control linear. According to this method the proposed time-step is calculated using the following formulation:

$$\textbf{Previous Time Step} * \frac{\text{Target Value}}{\text{Monitored Value}} \tag{3.43}$$

,where as target value has been set the $\frac{\text{Tube Thickness}}{10}$. Also, as monitored field the Max norm has been chosen that uses the maximum absolute displacement of the flexible tube. These simulations, using 32 cores on a single node, took one hour to complete.

3.3.2.2 FSI case with pressure gradient

The only difference in this FSI case compared to the previous one is that the fluid now has different pressures at the inlet and outlet. In this case, an attempt was made to replicate Gregory's experiment. The same pressure ramp formula used for Pexternal was applied at the inlet of the experiment. Also here the time step was from 0.001 to 1 second and it was changing with the adapting time step method as

in the previous simulation. These simulations, using 32 cores on one node, took 7 days and still the tube didn't reach the buckling state.

3.3.2.3 Symmetrical FSI case without pressure gradient

The FSI case involving fluid pressure appeared to be highly time-consuming, potentially endangering the thesis deadline. As a result, the next step was to create a new symmetrical FSI case where the tube and the entire experiment layout were cut in half. The only change in the boundary conditions was that the surfaces at y =0 were set to be symmetrical. Again the first FSI case was without fluid pressure to check if the simulation is working properly.

Now that the entire layout is cut along the y-axis, the method for creating the fluid domain needs to be slightly adjusted. First, an additional surface block containing the tube was created. Then, using the subtract command, the tube's interior was extracted, and the process continued as in the previous FSI cases. The subtraction is illustrated in figure 3.8.

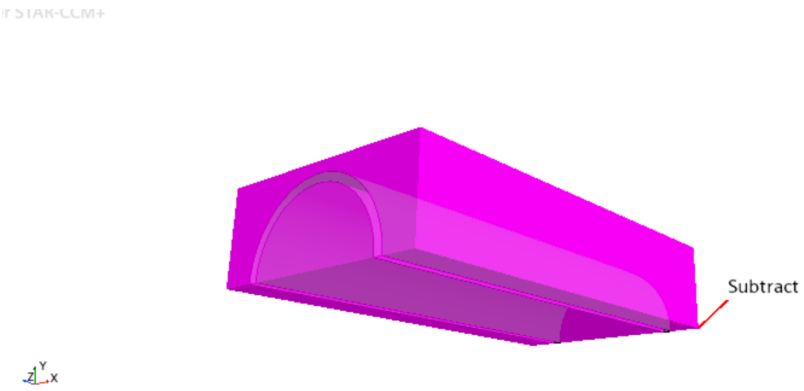

Figure 3.8: Subtracted block

To simplify the runs, the remeshing solver in Star-CCM+ was utilized in these new FSI cases. This solver automatically remeshed the entire fluid domain during specific events. The chosen triggers for the remeshing were when the normalized area in the middle of the tube reached 0.75 and then 0.5, decreasing by 0.5 with each step down to 0.05. With this setup, manual remeshing was no longer necessary.

3.3.2.4 Symmetrical FSI case with pressure gradient

Once the symmetrical case without fluid pressure was functioning correctly, a new attempt was made with a symmetrical case that included fluid pressure. However, the simulation proved to be unstable and couldn't progress beyond the tube's buckling state, which will be further discussed in the results. This led to the need for a different approach. In the final simulation, the boundary conditions were altered. Instead of using pressure at both the inlet and outlet, the new setup involved a velocity inlet and a pressure outlet. The inlet velocity was set to 10 m/s, as suggested by Laudato [46]. Another adjustment made was the use of Simcenter STAR-CCM+'s

dynamic stabilization method for the FSI cases. After some experimentation, the chosen dynamic coefficient was $100 * \text{tube's inner diameter}$. In the earlier FSI simulations with the pressure inlet, the dynamic stabilization method proved ineffective, so an under-relaxation method with a coefficient value of 0.2 was employed instead. However, this alternative stabilizer also failed to work. These adjustments improved the stability of the simulation.

To capture the various phenomena occurring within the fluid inside the tube during the experiment and to explain the mechanism behind the wheezing, numerous reports were generated, and multiple points and surfaces were placed within the fluid and along the tube walls.

More specifically, the points within the fluid domain were strategically selected to capture vortices, pressures, and velocities, providing insights into potential phenomena. Their locations are shown in Figures 3.10 and 3.11.

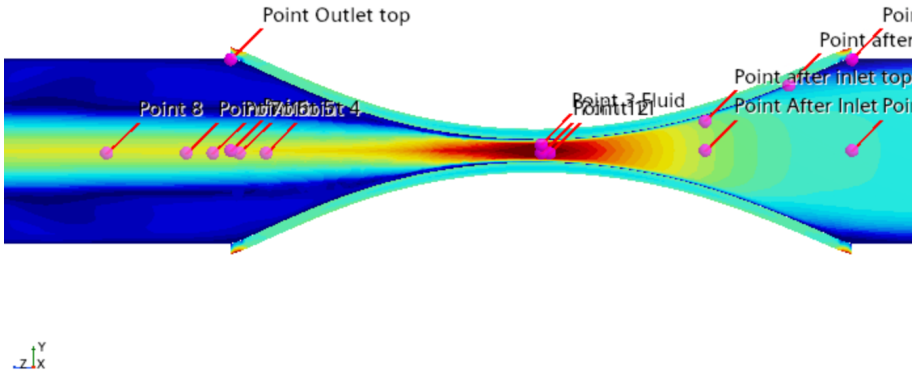

Figure 3.9: Fluid points normal to x axis

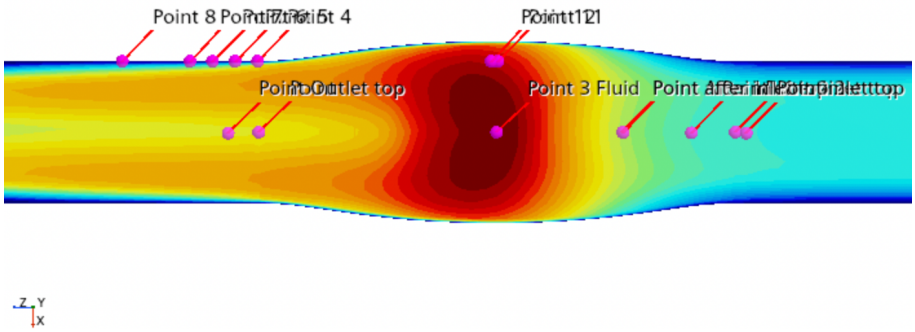

Figure 3.10: Fluid points normal to y axis

The same approach was applied to the tube. Points were placed within the tube walls to measure wall displacement. The recorded displacement data was then processed using a MATLAB script, which employed an FFT algorithm to extract the frequencies of the oscillations observed from the displacement. The locations of these points can be seen in figure 3.12.

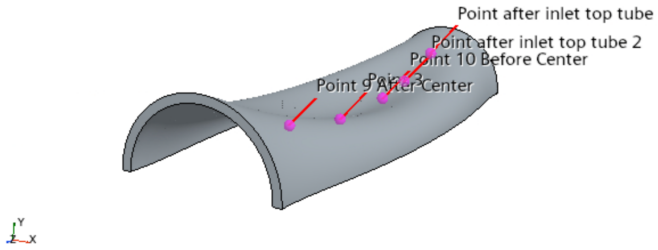

Figure 3.11: Tube points

The reports generated recorded pressure, density, velocity, vorticity, dynamic pressure, and mass flow rate at these specific points, as well as across certain entire areas or surfaces. Additionally, the Pprime was calculated, representing the pressure perturbation from the mean value. This can be determined by

$$P_{prime} = P - P_{mean} \tag{3.44}$$

where Pmean denotes the average pressure field. The calculation of Pprime is significant as it can reveal acoustic and hydrodynamic, aerodynamic waves that may arise. Also, key properties were computed, such as the Reynolds number and the ratio of dynamic pressure of the fluid to the external pressure at the tube, for comparison with Gregory's thesis and other related studies.

Finally, to ensure a stable simulation, a first-order scheme was selected, with a maximum of 50 Newton steps and a single load step for the fluid-solid coupling. The "dynamic" method was chosen for stabilization, with a convergence tolerance of 1e-64. For the segregated flow, the velocity under-relaxation factor was set to 0.8, and the pressure under-relaxation factor was set to 0.2.

4
Results - Discussion

On this sections the results of the thesis will be presented and they will be discussed in detail.

4.1 Solid cases

Firstly, the results of the three goals of the solid cases will be presented.

4.1.1 Validation of tube law for solid cases

Below the normalized version and non of the tube law is being presented for Gregory's tubes that have been chosen for the solid cases of this thesis.

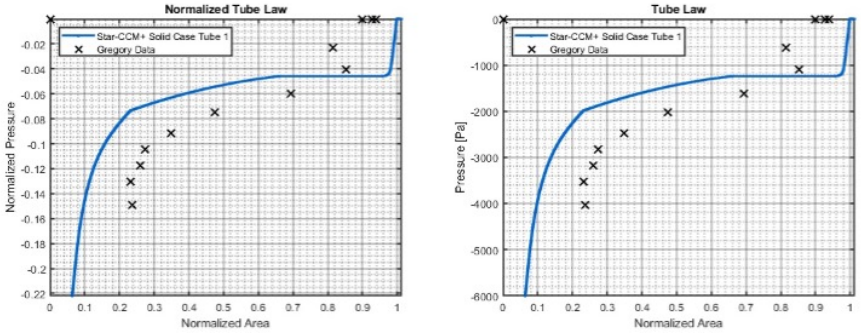

(a) **(b)**

Figure 4.1: (a) Normalized Tube Law for Tube 1, (b) Tube Law for Tube 1. In both cases the plot is the same. The simulation represents the tube as more flexible than in reality.

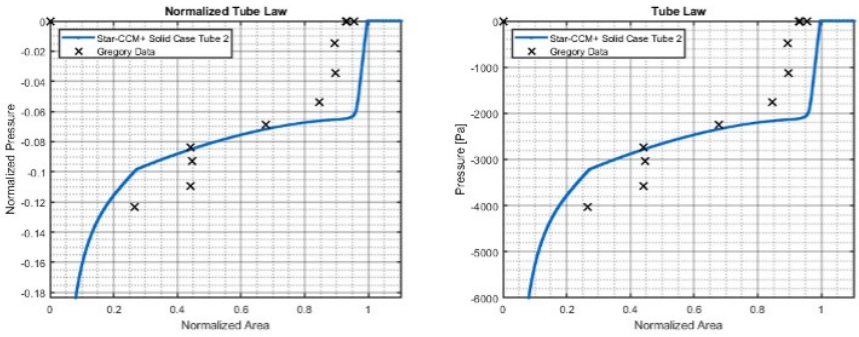

(a) **(b)**

Figure 4.2: (a) Normalized Tube Law for Tube 2, (b) Tube Law for Tube 2. In both cases the plot is the same. The simulation here is more accurate than tube 1, it just represents the tube as more flexible than in reality at the contact phase.

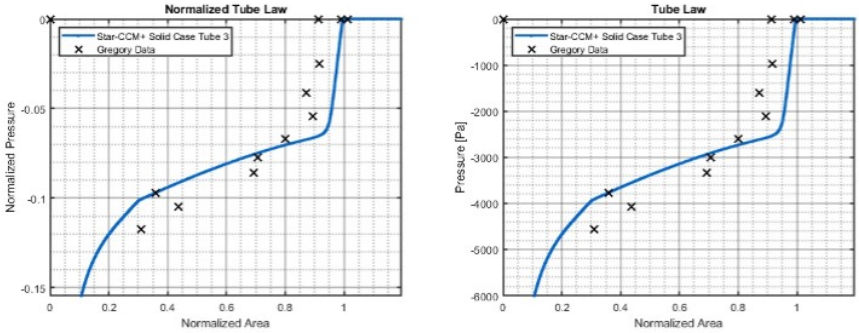

(a) **(b)**

Figure 4.3: (a) Normalized Tube Law for Tube 3, (b) Tube Law for Tube 3. In both cases the plot is the same. It is similar with tube 2.

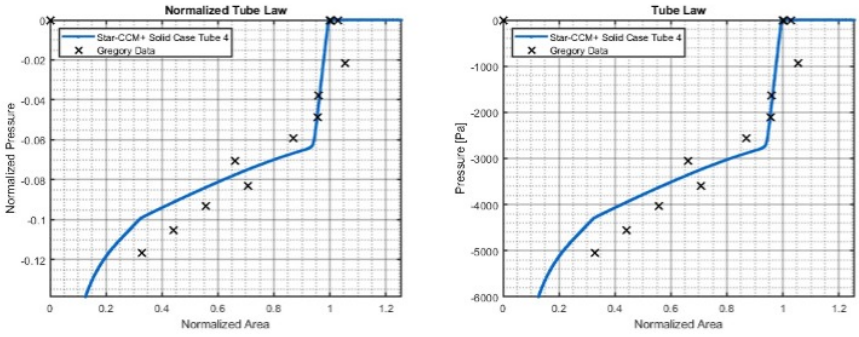

(a) **(b)**

Figure 4.4: (a) Normalized Tube Law for Tube 4, (b) Tube Law for Tube 4. In both cases the plot is the same. Similar with tube 2 and 3.

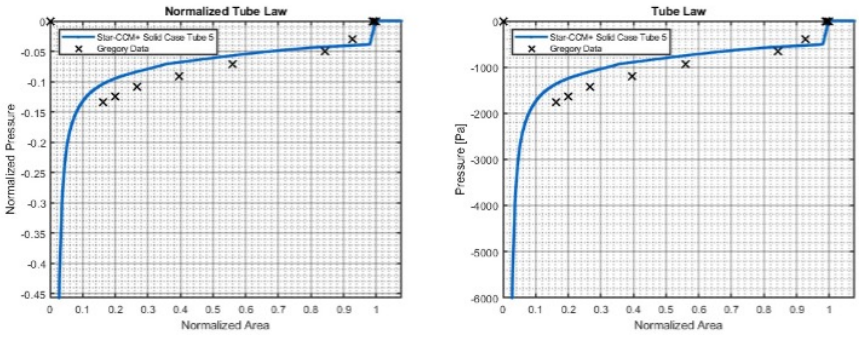

(a) **(b)**

Figure 4.5: (a) Normalized Tube Law for Tube 5, (b) Tube Law for Tube 5. In both cases the plot is the same. This tube is thinner and has bigger diameter than tube 1-3. The simulation represents the tube as more flexible than in reality.

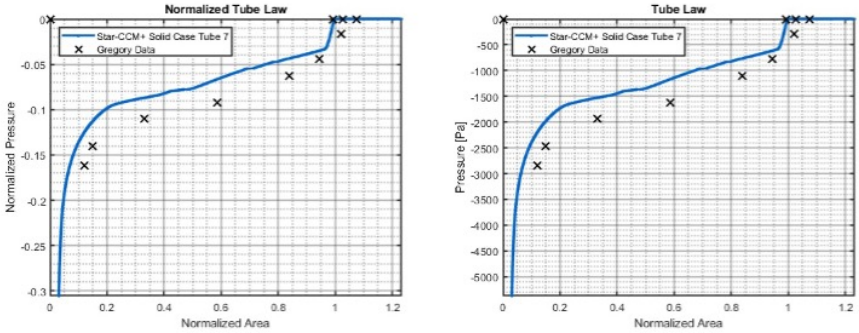

(a) **(b)**

Figure 4.6: (a) Normalized Tube Law for Tube 7, (b) Tube Law for Tube 7. In both cases the plot is the same. Similar with tube 5.

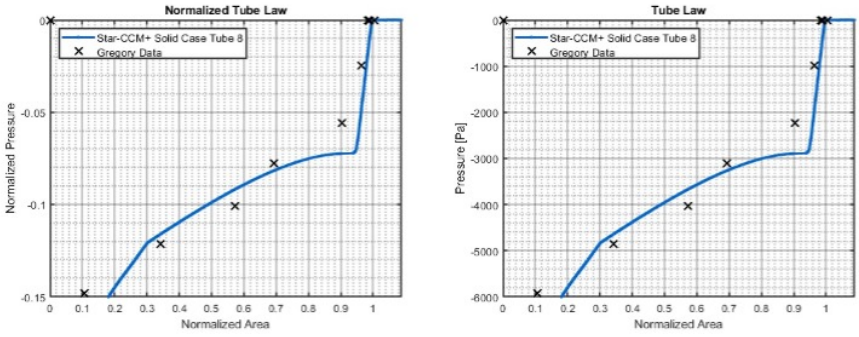

(a) **(b)**

Figure 4.7: (a) Normalized Tube Law for Tube 8, (b) Tube Law for Tube 8. The only difference of this tube with tubes 1-3 is that has smaller length. It is similar with tube 2 and 3, but at the contact phase makes the tube appears stiffer.

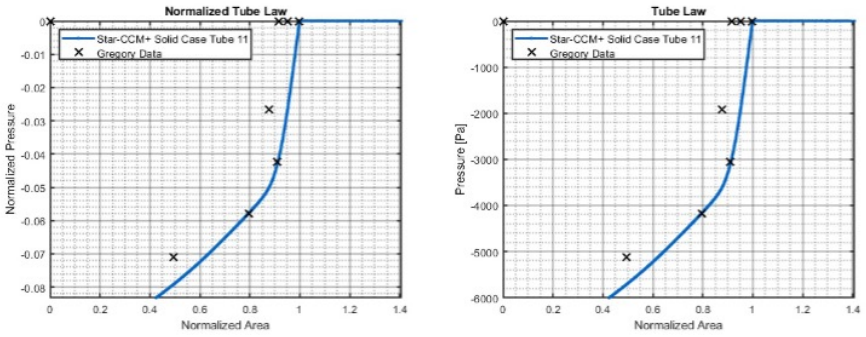

(a) **(b)**

Figure 4.8: (a) Normalized Tube Law for Tube 11, (b) Tube Law for Tube 11. In both cases the plot is the same. Similar with tube 8.

The shape and position of the tube law curves generated by the simulations closely correspond to the experimental data for the majority of tubes examined. A common observation across Figures 4.1 to 4.8 is that the simulated tube law consistently begins at normalized area values exceeding one. This discrepancy may be attributed to the precision limitations of the position data for the 30 points recorded from Star-CCM+. Increasing the number of recorded points might result in the normalized area starting at 1, as expected.

Tubes 1, 2, 3, and 4 belong to the first category of Gregory's tubes [1]. They share the same properties, with the only difference being their strained length L. Looking at the results, it can be seen that for almost all the tubes, the simulation's tube law curve matches the experimental tube law very closely.

However, the worst-performing curve is visible in Figure 4.1 for tube 1. Here, the simulation curve sits above the experimental data. This discrepancy might be due to the hyperelastic model is being used for the solid cases. It seems this model isn't quite accurate enough and makes the material appear more flexible than it really is. As a result, the simulations show the tube deforming more than it would in real life, especially at lower external pressures.

The same pattern observed with tube 1 can be seen in the second category of tubes, which includes tubes 5 and 7. It's noted that the simulation curve exceeds the experimental data in these cases. What sets these tubes apart is their thickness, which is half that of the first category, and their diameter, which is 1.07 times larger. Due to these differences, it's likely that these tubes are more challenging to model using the Neo-Hookean hyperelastic model compared to the first category.

To address this, it might be necessary to consider alternative approaches. A different hyperelastic model, such as Ogden, could be employed, as it allows for more strain-stress data of the material to be imported. Additionally, experimentation with other numerical models and mesh methods might be worth exploring. These steps could potentially lead to more accurate simulations for this category of tubes.

The final category of tubes, consisting of tubes 8 and 11, is characterized by properties similar to those in the first category, with one key difference: their initial length L_0 is reduced by 3 mm. A pattern comparable to that of the first category can be observed when the simulation curves are examined alongside the experimental data.

However, an interesting phenomenon is noted at the end of the curve for both tubes. It appears that the simulated tubes become stiffer than their real-life counterparts, resulting in smaller deformations. One possible reason for this discrepancy could be the enforcement of penalties on the center plate, which prevents the mesh elements from one side of the tube from penetrating the other side. Further analysis should be conducted to find optimal values for the contact gap and penalty enforcement, in order to bring the curve closer to the actual data. Another reason that this discrepancy might be attributed to limitations in the hyperelastic model being used. It's possible that the model may not be sufficiently accurate to capture the complex interactions occurring during the contact phase.

Based on the above results, it can be seen that the solid simulations are reliable because the results closely match Gregory's experimental data [1]. This suggests that the mesh, solid models, settings, boundary conditions, and the New-Hookean hyperelastic model are suitable for simulating the buckling and contact phase of these starling resistors. It should be noted that Laudato's tube laws are more similar to Gregory's data than these solid simulations [45]. The mesh used in this study is the same as Laudato's, so the discrepancy must lie elsewhere. This could be due to the method used to extract the tube deformation for calculating the tube law or the use of certain unknown parameters in the simulation. Still, the solid simulations can be considered valid when compared to Gregory's data because the deviation of the simulation curve from the real data is minimal.

4.1.2 Mid side vertex with linear interpolation

The last part of the solid cases is showing how the mid side vertex with linear interpolation on Star-CCM+ might help to have more accurate results.

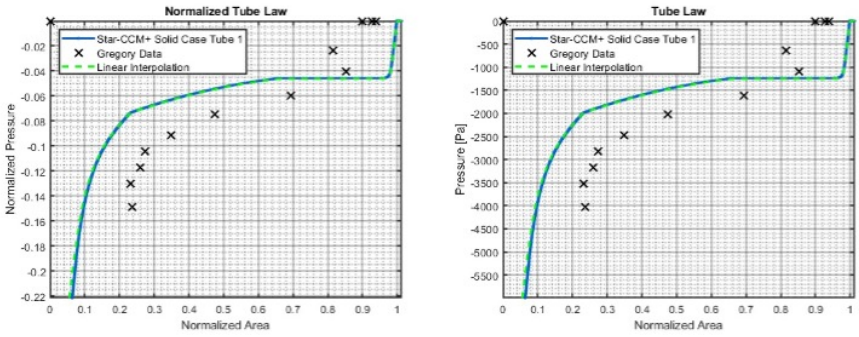

(a) a **(b)** b

Figure 4.9: (a) Normalized Tube Law for Tube 1 comparison with and without linear interpolation, (b) Tube Law for Tube 1 comparison with and without linear interpolation

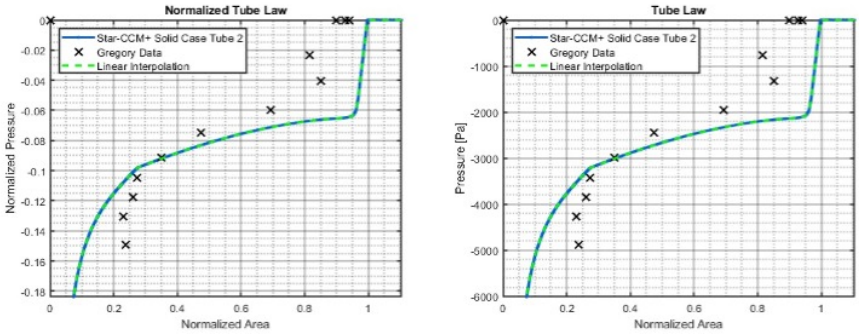

(a) a **(b)** b

Figure 4.10: (a) Normalized Tube Law for Tube 2 comparison with and without linear interpolation, (b) Tube Law for Tube 2 comparison with and without linear interpolation

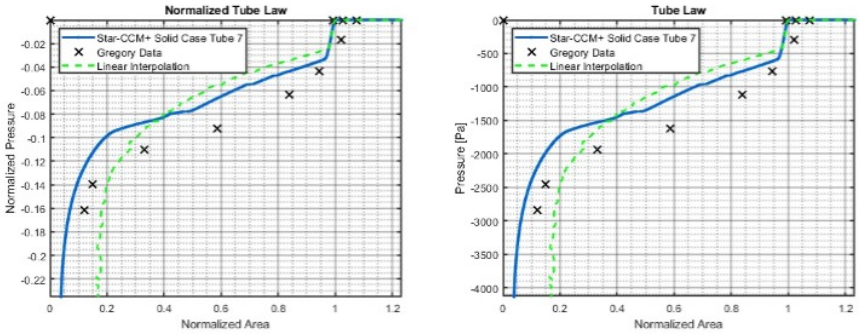

(a) a **(b)** b

Figure 4.11: (a) Normalized Tube Law for Tube 7 comparison with and without linear interpolation, (b) Tube Law for Tube 7 comparison with and without linear interpolation

In figures 4.9 and 4.10, it was observed that there was no difference in the solution for tubes 1 and 2, which fall under the first category, when compared to the solution without the mid side vertex. However, for tube 7, which belongs to the second category and has thinner walls, it was noticed that the extra point that is being added by the interpolation caused the curve to fall below the experimental data during the contact phase. This resulted in the tube exhibiting greater stiffness. A possible explanation is that the geometry is being represented with more cells in the curves of the geometry than the original version of the tube, and it might keep it stiffer under the external pressure.

4.2 FSI cases

On this section, we will present the results of the FSI cases which is the combination of the solid cases with the difference that now fluid passes through. As mentioned in the methods section, only tube 2 has been selected for FSI cases due to its valid results in the solid case.

At the beginning, in the FSI cases, the same elleptical geometries from solid cases has been used to achieve two lobes buckling. But in fig 4.12 and 4.13 can be seen that this wasn't the expected result.

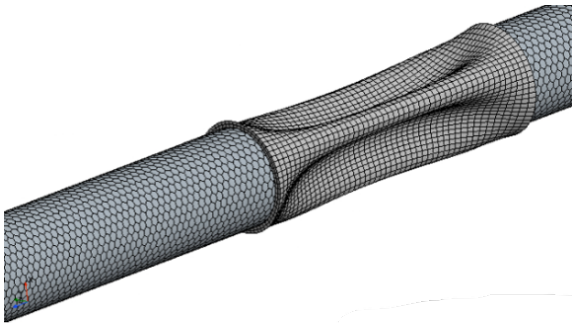

Figure 4.12: Three Lobes Buckling of the elliptical Tube 2 in FSI case

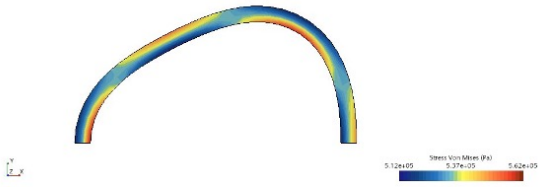

Figure 4.13: Three Lobes Buckling of the mid section of the elliptical Tube 2, at xy

The external pressure does not act symmetrically on the tube, possibly due to the locking of mesh elements. To solve this issue, the perturbation force has been used in the rest FSI cases, as it has been explained in methods. Now the tube 2 that

is being used is circular like Gregory's experiments. Figure 4.14 shows how the perturbation force, solves asymmetrical issue.

Figure 4.14: Two Lobes Buckling of mid section of the circular Tube 2, at xy, with perturbation force.

4.2.1 FSI case without pressure gradient

On this simulation there is no pressure difference at the fluid domain, the fluid moves only with the deformation of the tube.

4.2.1.1 Validation of tube law

The tube law of tube 2 can be seen in fig. 4.15

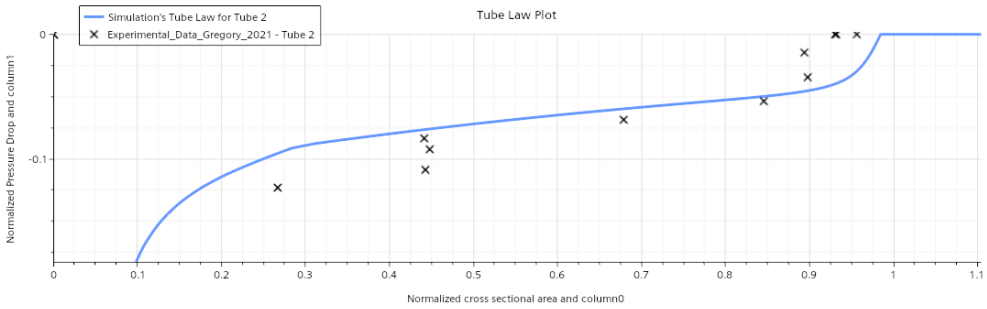

Figure 4.15: Normalized tube law of tube 2 in FSI Case

The results indicate that the tube model aligns closely with the experimental data, albeit slightly less accurately than the solid model. The tube model consistently exceeds the experimental data, as observed in the case of tube 1 in the solid models. This suggests that the FSI model makes the tube more flexible, causing it to deform under lower external pressures than occur in reality. Consequently, this simulation does not align well with Gregory's experiments, as the fluid movement is solely attributed to the tube's deformation [1]. Therefore, an FSI model incorporating fluid pressure in the fluid domain is necessary. But figure 4.15 demonstrates that the FSI simulation has achieved its goal. The simulation is valid as the curve closely matches the experimental data even without fluid pressure.

4.2.2 FSI case with pressure gradient

As mentioned in the method, in this FSI case, there is a pressure difference within the fluid domain between the inlet and the outlet due to the pressure ramp of the external pressure at the inlet.

4.2.2.1 Progress

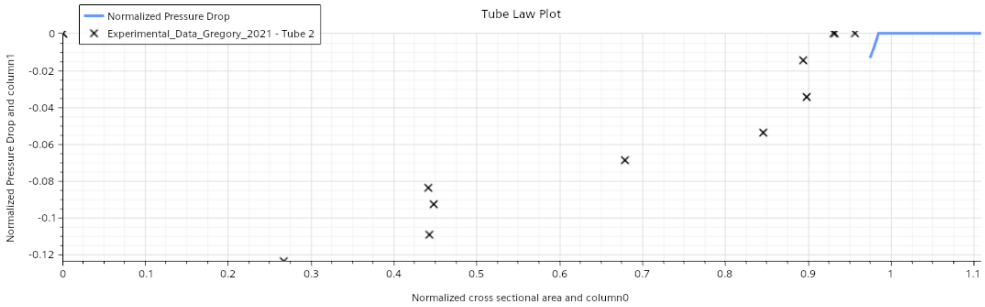

Figure 4.16: Normalized tube law of tube 2, FSI case with pressure gradient

The plot in Figure 4.16 displays the progress of a simulation that has been running for five days using 32 cores and a time step of 0.001 seconds. It is evident that the simulation did not even reach the buckling phase, indicating that it might take several weeks to complete if everything was working perfectly. To address this issue, a new symmetrical case has been implemented, as described in the methodology.

4.2.3 Symmetrical FSI case without pressure gradient

On this subsection is the symmetrical FSI case. The boundary conditions are being mentioned in methods.

4.2.3.1 Validation of tube law for symmetrical FSI case

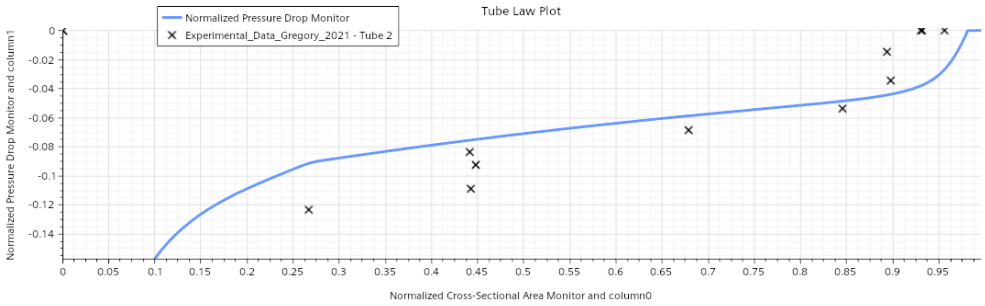

Figure 4.17: Normalized tube law of symmetrical tube 2 without fluid gradient

From Figure 4.17 can be seen that the tube law is exactly the same with the Figure 4.15. That validates that the simulation runs correctly without fluid pressure. The next step was to create the symmetrical FSI case with fluid pressure.

4.2.4 Symmetrical FSI case with pressure gradient

This subsection is the last and most important one, as it fulfills the goals of the thesis. The first symmetrical FSI case created used a pressure difference for bound-

ary conditions, following Gregory's experiment [1]. This FSI case was found to be unstable and it was diverging at the buckling state of the tube. Many different techniques were attempted to stabilize the simulation, but ultimately did not work. For more details, refer to the following sections. The only solution was to use a different boundary condition for the inlet. Therefore, the next and final FSI case uses velocity instead of pressure as the input at the inlet. As explained earlier in the methods section, the velocity value is fixed at 10 m/s [46]. In the FSI case with pressure difference as a boundary condition, the pressure was increasing at every time step, which led to the velocity increasing at every time step.

4.2.4.1 Symmetrical FSI case with pressure gradient as boundary condition

As said above the simulation with pressure gradient as boundary condition, it diverges at the buckling phase. Suddenly, the tube law goes straight, and the tube has huge deformations. The tube starts oscillates back and forth nonphysically.

To solve this issue, many different things have been used, like different stabilization methods, different FSI coupling specification and different time steps.

To stabilize the simulations, both the Dynamic and Relaxation methods were used. The relaxation coefficient was set to 0.2 or 0.1, and for the dynamic method, the inner tube diameter or 100 times this diameter was used as the dynamic coefficient to enhance stability. Also, a different hyperelastic model, the Ogden model, has been used instead of the New Hookean model. Ogden is generally a more accurate model, especially when strain stress data of the material is imported [67]. It has been chosen because it could potentially model the tube law of the material more accurately and smoothly, leading to a more stable simulation.

Additionally, a small time step was utilized to slow down the simulation and reduce radical deformations of the tube. Different FSI coupling specifications were tested, including Pressure or Pressure with Shear Stress. While the second is more accurate, the first is simpler for coupling and might have helped to stabilize the simulation. The appendix contains a larger table, showing various strategies employed to stabilize the simulation.

Another consideration was the choice between first and second order scheme. The first order was selected mainly for its simpler solving. Moreover, instead of the classic boundary condition, where pressure increases at the inlet, a new boundary condition was tested, keeping stable the pressure at the inlet while gradually decreasing it at the outlet, following the pressure ramp of the external pressure.

Furthermore, the Young Modulus of the tube was adjusted to make it stiffer when the acceleration of the displacement of the tube wall was significant, in order to reduce it. The equation that has been used to adjust the Young Modulus was

$$Y_0 * (1 + (\frac{a_t - a_c}{a_c})^2) \tag{4.1}$$

, where Y_0 is material's initial young modulus 1MPa, a_c is the critical acceleration and a_t is the acceleration. So when the acceleration goes above the a_c the equation 4.1 is activated and it increases the Young Modulus of the material.

Unfortunately, none of these techniques made the simulation stable. Each one of them diverged at the buckling state of the tube. A possible explanation is that the pressure difference was increasing per time step, causing the velocity to increase with each time step. As the tube closed and took on a venturi tube shape, the area in the middle section of the tube decreased, causing the fluid to accelerate. The speeds of the fluid had velocities higher than 0.2 Mach, which according to literature was wrong. This led to increased forces from the fluid to the tube walls, resulting in significant deformations close to the buckling phase. These deformations made the simulation unstable. Something that wasn't tested is to use a pressure outlet giving probably better stability with imposed pressure.

That's why a new boundary condition with stable velocity at the inlet have been tried.

4.2.4.2 Validation of tube law of the FSI case with velocity inlet as boundary condition

To validate this FSI simulation with velocity inlet as a boundary condition, a time step of 0.001 sec has been used, which is big enough to check the result fast. First order has been used as a solving scheme to keep it simple and the ogden hyperelastic model.

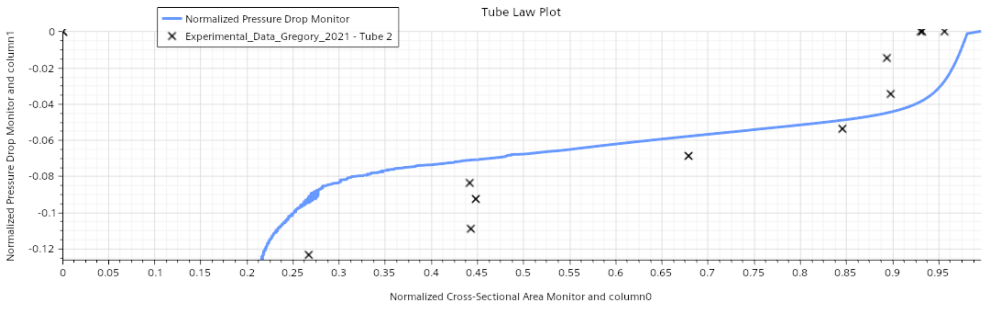

Figure 4.18: Normalized Tube Law for Tube 2, Symmetrical FSI Case

In Figure 4.18, it can be observed that the simulation runs until the point when the contact phase of the tube starts. For most of the experiment, it is stable, and then it diverges. The velocity inlet, as a boundary condition, worked and made it more stable. Comparing to the symmetrical FSI Case without fluid pressure in Figure 4.17, it behaves much better close to the contact phase. The tube is stiffer and closer to the experimental data. This tube law that is being produced seems valid, making the simulation suitable for further analysis, especially to capture oscillations, as they occur slightly before the contact phase, which this simulation covers. Also, it will be tried to explain the mechanism that produces the wheezing.

Additionally, the second order scheme has been tried, but the simulation diverged earlier than the one with first order scheme. It can be seen in Figure 4.19

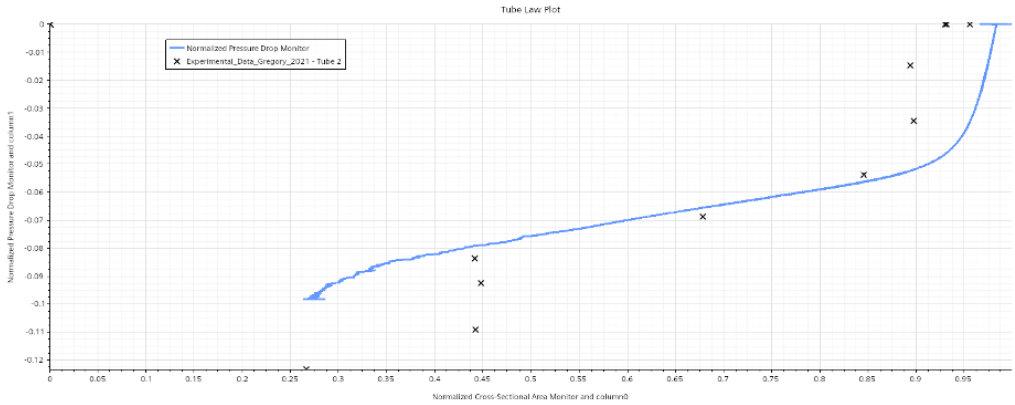

Figure 4.19: Normalized tube law of tube 2 with second order scheme, for symmetrical FSI case

This probably occurs, because the second order is increasing the complexity of the calculations and the error in the residuals is bigger and at some point the simulation diverges.
Finally, it is worth mentioning that instead of using laminar flow, the turbulent k-w model (SST) was employed to determine if the tube law is more effective.

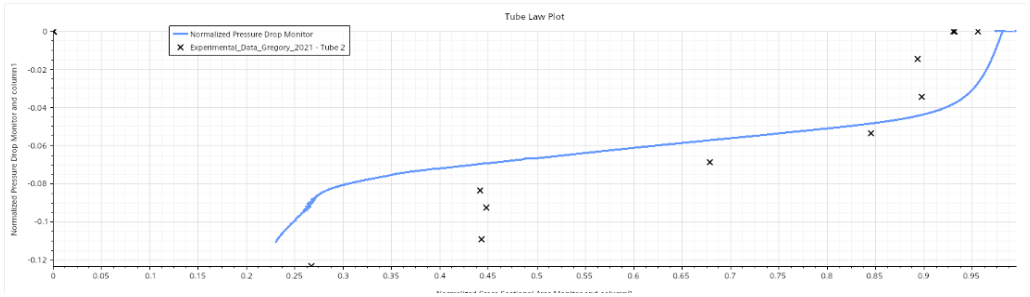

Figure 4.20: Normalized tube law of tube 2, with turbulent model K-W (SST)

By comparing Figure 4.20 with Figure 4.18, it is observed that the simulation using the turbulent model at the end of the curve shifts more to the left compared to the simulation with laminar flow. This indicates a decreased level of accuracy. This discrepancy could be attributed to the need for a better-designed fluid domain mesh for the SST model, ensuring correct y+ values for the mesh elements.

4.2.4.3 Mechanism of oscillations

This chapter is important because we will now discuss a potential mechanism for wheezing based on the valid simulation results. From the theory section, there are many different theories for this mechanism, but none of them has been proven valid so far. Some theories suggest that sloshing causes the tube to start oscillating, while others propose that a symmetry breaking of the flow downstream and

vorticity waves can make the tube oscillate. The vorticity waves might create instabilities in wall motion due to shear layer instabilities. Another possible mechanism is that the formation of a constriction in the middle section of the tube leads to increased upstream pressure that exceeds the opposing chamber pressure, resulting in the opening of the constriction and causing the tube's oscillation. So, in order to observe what is going on, a strategy with many different points and surfaces has been followed as discussed in the methods.

In these simulations, as mentioned previously, the inlet velocity is consistently 10 m/s. As shown in the Figure 4.21, the velocity increases as the neck of the tube narrows due to the venturi effect and can reach values of 0.1 Mach which is valid according to literature [24]. Additionally, the Reynolds number in Figure 4.22, which is above 200, indicates that oscillations are expected to occur. According to literature, stronger oscillations are anticipated as the Reynolds number increases, signifying increased fluid turbulence. The time step currently being used when oscillations occur is 0.00003 seconds. This value has been selected to capture Gregory's frequencies [1]. Gregory stated that the frequency at the start of the oscillations is 164 Hz. In order to capture this frequency, the time step must be 1% of the period of the Nyquist frequency, which is 328 Hz, equivalent to 0.00003 seconds.

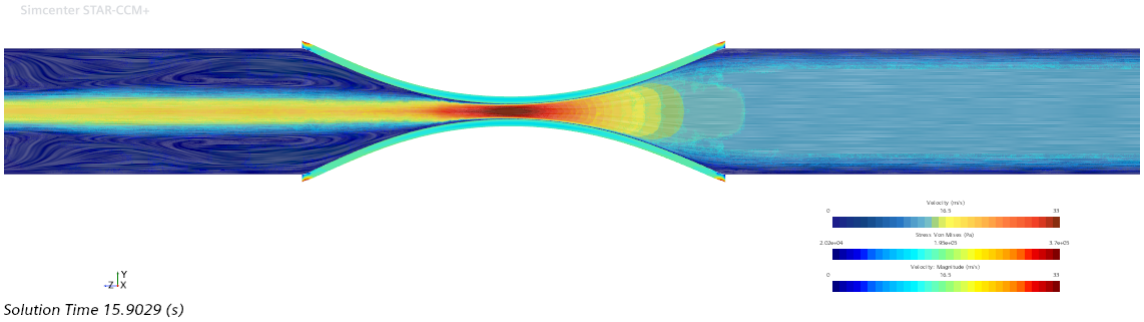

Figure 4.21: Velocity at main longitudinal cross section

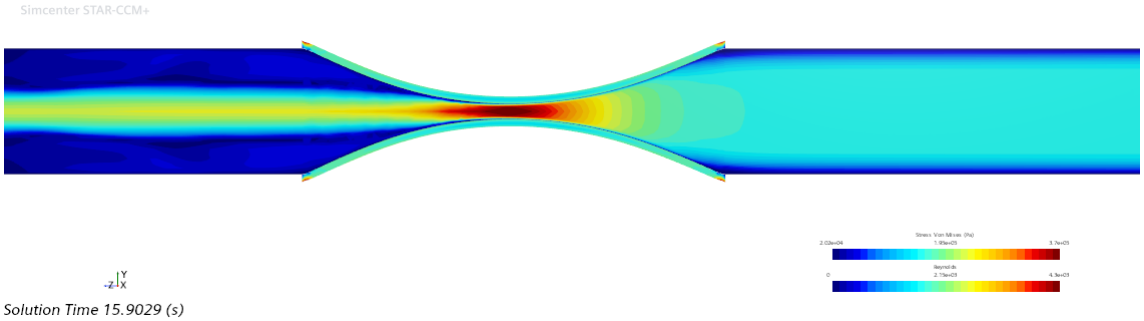

Figure 4.22: Reynolds Number at main longitudinal cross section

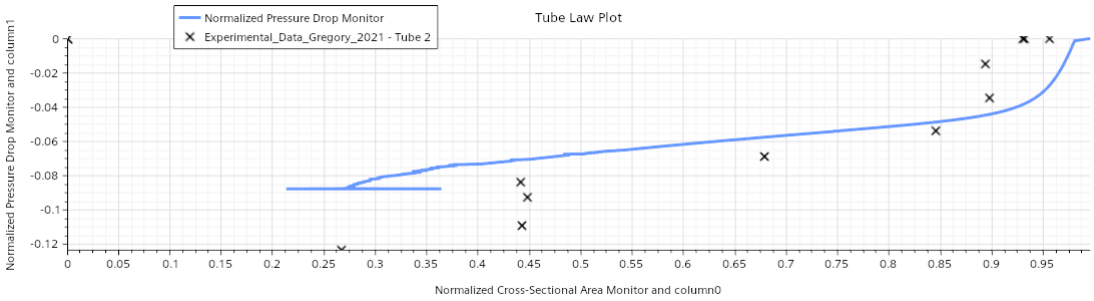

Figure 4.23: Normalized Tube Law of Final FSI Simulation

In Figure 4.23, the tube law of the final simulation is depicted, which attempts to replicate Gregory's oscillations [1]. It can be observed that after the tube has passed 0.5 of the normalized area, it begins to oscillate because the curve of the tube law fluctuates back and forth along the x-axis. The issue arises near the contact phase, where it diverges with this time step, unlike what is seen in Figure 4.18 with a larger time step. As a result, this simulation can capture oscillations only before the contact phase, but hopefully, this area might be sufficient to thoroughly comprehend the wheezing mechanism.

Before analyzing the frequencies of these oscillations, the eigenvalues of the material must be presented to check if the material has the flutter effect during the oscillations. The eigenvalues can be seen in Figure 4.24 tp 4.26.

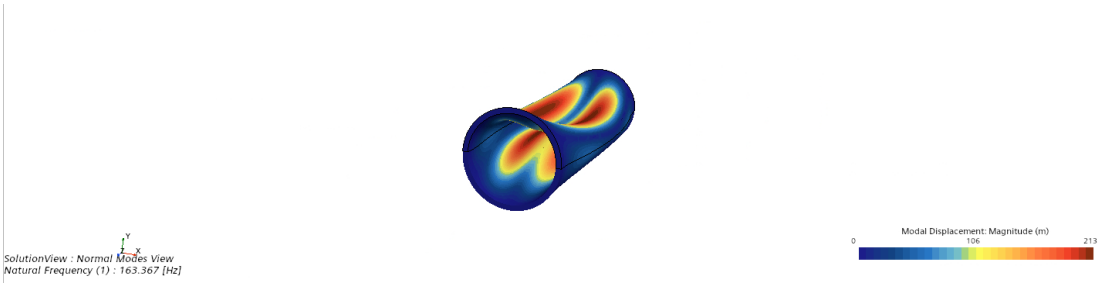

Figure 4.24: Normal Mode 1 of Tube 2

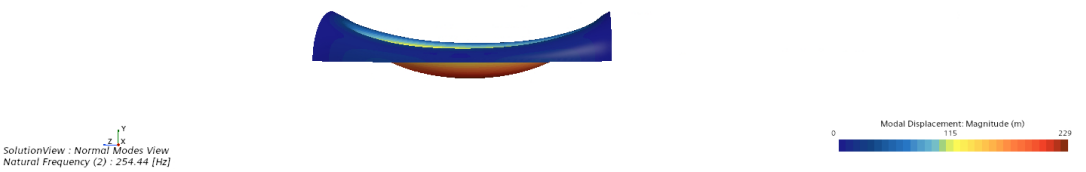

Figure 4.25: Normal Mode 2 of Tube 2

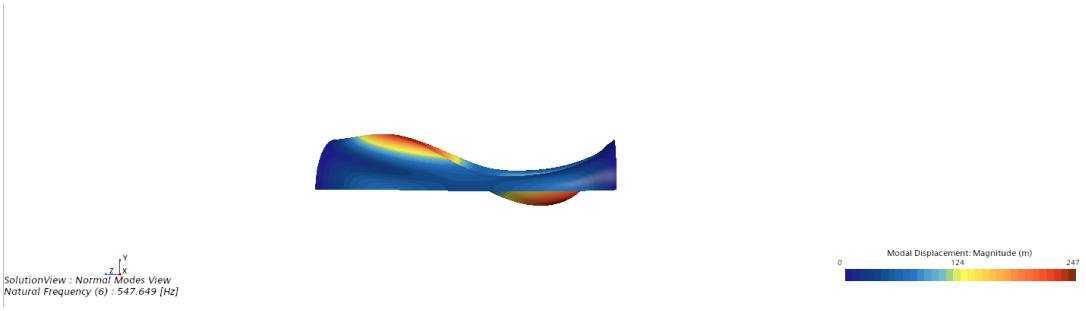

Figure 4.26: Normal Mode 6 of Tube 2

It is clear that in the first normal mode, the natural frequency is almost 164 Hz, which matches Gregory's frequency at the start of the oscillations [16]. Gregory explains that the oscillations result from a combination of two modes: normal mode 2 and normal mode 6. This combination of normal modes can cause the tube to experience a flutter effect. The natural frequencies of these normal modes are 254 Hz and 547 Hz, respectively.

Let's delve deeper into the frequencies of the oscillations in the simulation. The onset of the oscillations with Gregory's frequency isn't clear where exactly appears. So a small range of the displacement of the point that is within the walls of the tube in the middle section close to the possible onset is being used.

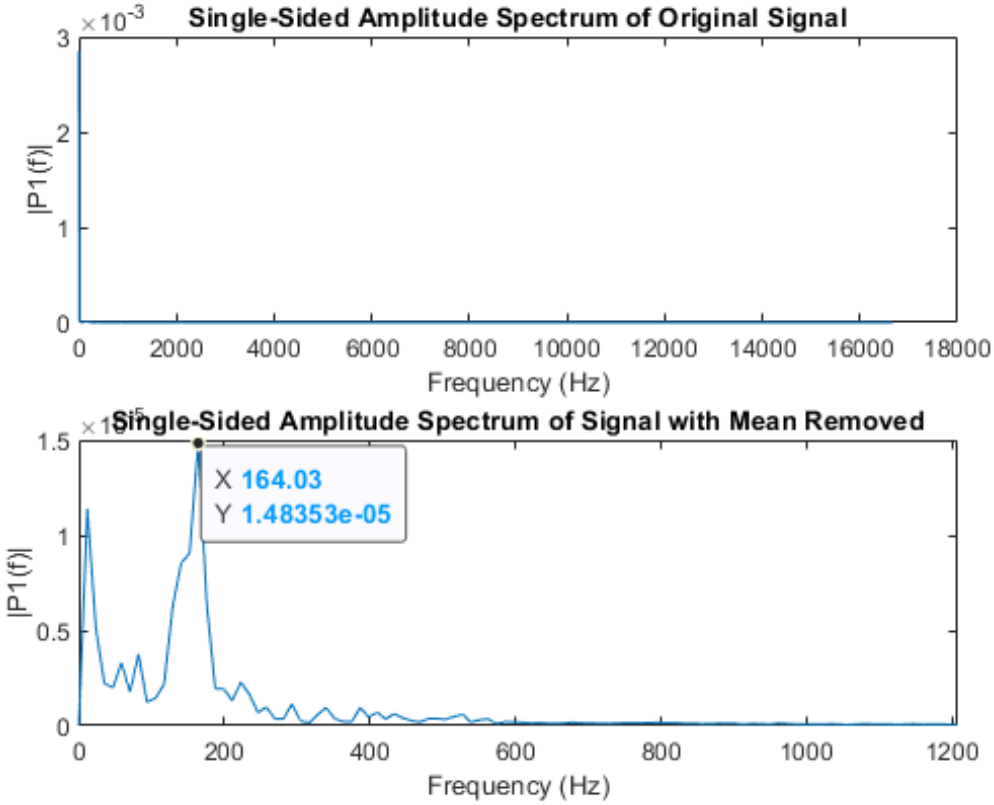

Figure 4.27: Frequency of 164 Hz close to a possible onset of the oscillations

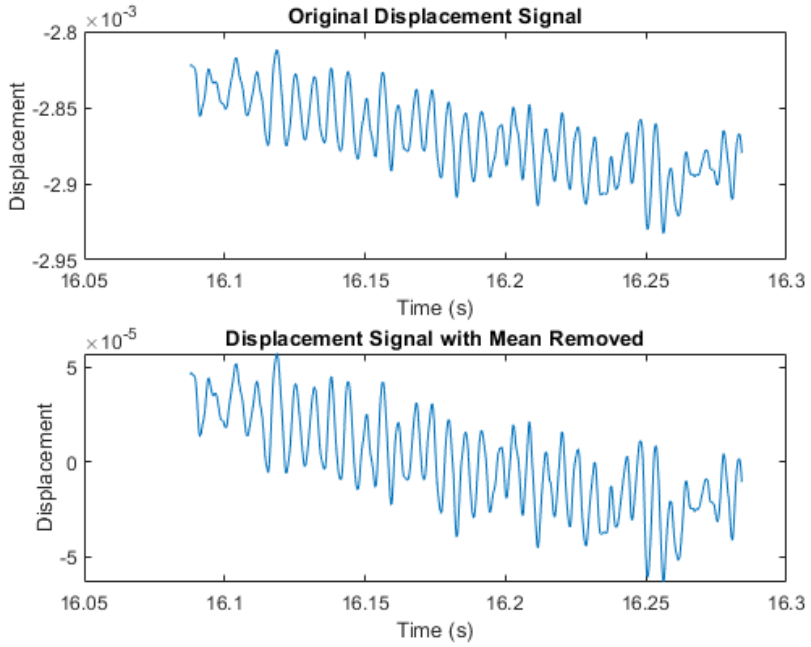

Figure 4.28: Displacement range of the 164 Hz frequency

The data from Figure 4.27 illustrates that the tube oscillates within a specific time range at a frequency of 164 Hz. Meanwhile, the information from Figure 4.28 indicates that the time range spans from 16.08769 to 16.203 seconds, when the external pressure is around 2464 Pa. Following this interval, there is a noticeable trend of increasing of the dominant frequency and decreasing magnitude of the oscillations. This prompts a more thorough investigation to determine the cause of this change and to pinpoint the onset of the oscillations.

Table A.2 in the appendix showing the observations of the oscillations under investigation. The investigation began at 15.4 seconds when the downstream flow became asymmetrical, and this will be explained in detail later. At 15.4 to 16 seconds, it was noticed that the tube was vibrating most at 133 Hz, with smaller peaks at 148 Hz and 168 Hz. This pattern continued until 16.024 seconds. Between 16.024 seconds and 16.06 seconds, the main frequency shifted between 133 Hz and 144 Hz, trending towards 144 Hz at around 16.06 seconds. After 16.06 seconds, the main frequency stabilized around 144-147 Hz, with the second highest frequency around 165-168 Hz. From 16.069 seconds onwards, the main frequency mostly hovered around 164-168 Hz and occasionally reached 179 Hz. From 16.102 seconds to 16.171 seconds, the main frequency varied between 164 Hz and 175 Hz. After 16.171 seconds, the main frequency increased and varied between 175 Hz and 200 Hz. The simulation diverges when the tube oscillates at 380 Hz.

The following findings indicate that the tube begins to oscillate at around 133 Hz, after which the dominant frequency increases to 144 Hz, then to 164 Hz, and ultimately reaches 200 Hz by the end of the simulation. As the mid-section of the tube becomes narrower, the oscillation frequency of the tube increases. Also, examination

of Figure 4.27 reveals peaks near 254 Hz and 547 Hz. However, further investigation is necessary to determine whether the tube is experiencing the flutter effect.

The next point of this chapter is to understand how these oscillations occur. Firstly, Gregory mentions that at the onset of the oscillations the division of dynamic pressure with external pressure is around 0.2 - 0.3 and the P_{inlet} - $P_{External}$ increases [1]. On this simulation at 15.4 seconds suddenly the downstream flow breaks symmetry, and this is an indication that the oscillations probably begin at this point. This can be seen in Figure 4.29.

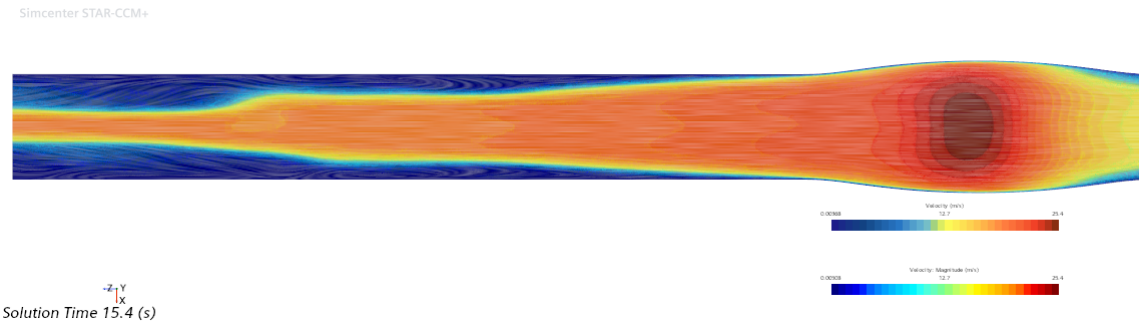

Figure 4.29: Velocity at main longitudinal cross section, Flow breaks symmetry at 15.4 seconds

General, asymmetry in a flow can occur due to uneven external forces such as gravity, non-uniform boundaries and wall conditions like roughness, an uneven pressure gradient across the flow field, asymmetric obstacles, variations in fluid properties such as density, viscosity, or temperature, turbulent flows, and the formation and interaction of vortices and eddies, and finally bifurcations [52], [34], [39], [46], [47], [59]. According to the literature, the most likely reason for this asymmetry is the occurrence of vortices and eddies in the mid-section of the tube [52], [34], [39]. It will be further investigated

Figures 4.30 shows the pressure at the inlet. Firstly, it can be seen that at 10 seconds there is a peak in pressure, this appears because then the fluid starts to move with a velocity of 10 m/s. Later the pressure stays stable at around 25 Pa and after 14.4 seconds starts to increase and at 15.4 second and later increases even faster. The oscillations of the curve at 15.4 second occur due to the smaller time step that is being used from this point and after. The smaller time step can catch more detail as it has been explained before. This pressure curve aligns with Gregory's observation that the oscillations begin when the P_{inlet} -$P_{External}$ increases [1].

Figure 4.31 presents the division of the dynamic pressure with external pressure. It can be seen that at 15.4 seconds is 0.175 and at 16.087 seconds where the 164 Hz appear as a dominant frequency of the oscillations the division has a value of 0.3 that aligns with Gregory's value [1].

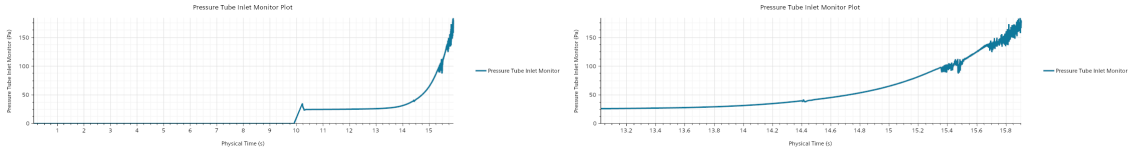

Figure 4.30: (a) Pressure at the inlet (b) Pressure at the inlet, zoomed

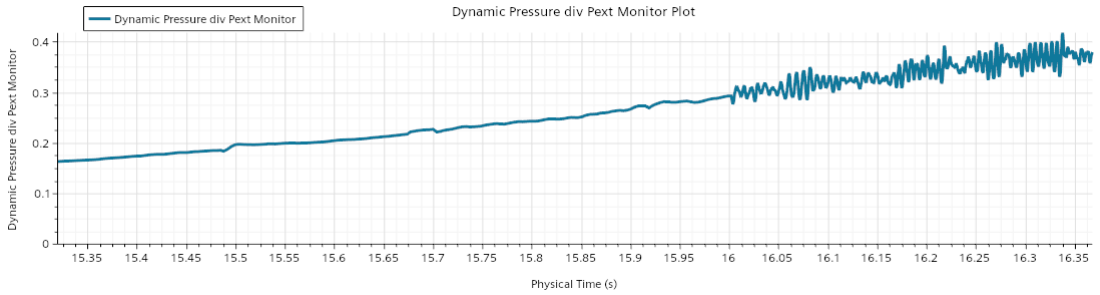

Figure 4.31: Dynamic pressure divided by external pressure

From these results, it can be said that the simulation is close to the experimental data, except from the validation of tube law. Now, the time range of 15.4 until the end of the simulation 17.15 seconds will be further investigated and hopefully a conclusion will be draw regarding the mechanism of wheezing.

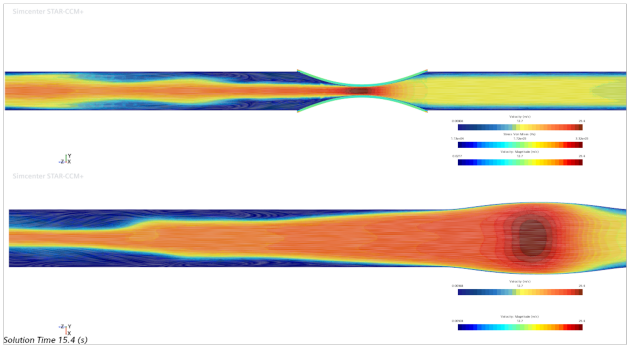

Figure 4.32: Mean axial velocity in the two main longitudinal cross sections of the domain at 15.4 seconds of the simulation. It can be seen that the flow breaks symmetry. The arrows have been created with line integral convolution of the velocity field and represent the mean velocity.

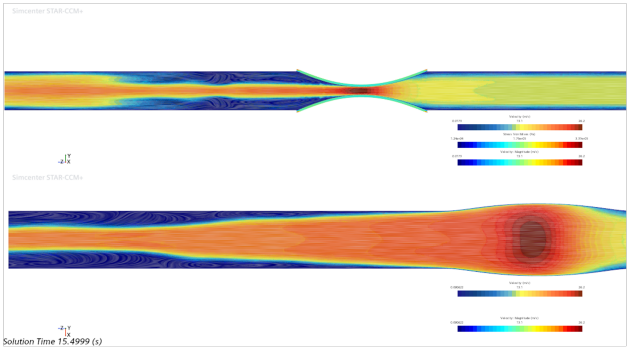

Figure 4.33: Mean axial velocity in the two main longitudinal cross sections of the domain at 15.5 seconds of the simulation. The flow at the downstream goes upwards. The arrows have been created with line integral convolution of the velocity field and represent the mean velocity.

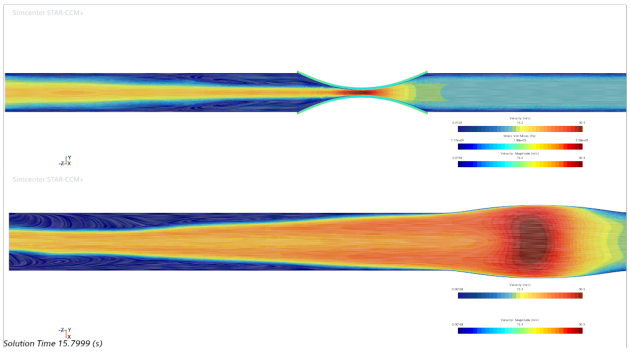

Figure 4.34: Mean axial velocity in the two main longitudinal cross sections of the domain at 15.8 seconds of the simulation. The flow at the downstream seems similar to the 15.4 seconds. The arrows have been created with line integral convolution of the velocity field and represent the mean velocity.

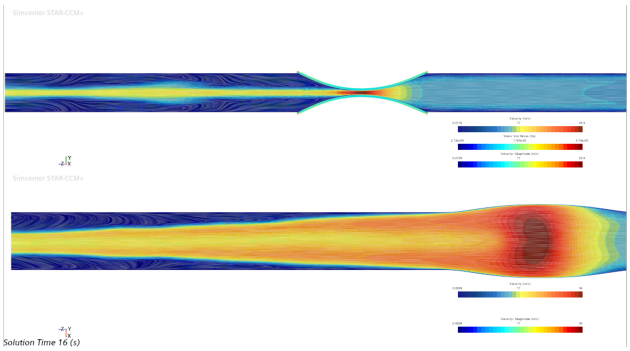

Figure 4.35: Mean axial velocity in the two main longitudinal cross sections of the domain at 16 seconds of the simulation. It can be seen that the flow starts to break in the middle. The arrows have been created with line integral convolution of the velocity field and represent the mean velocity.

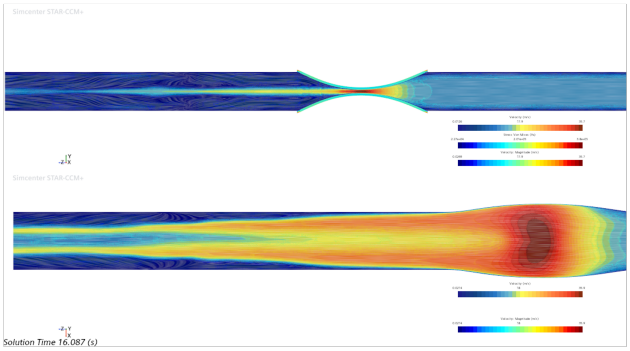

Figure 4.36: Mean axial velocity in the two main longitudinal cross sections of the domain at 16.087 seconds of the simulation, where the tube oscillates at 164 Hz. The separation becomes greater. The arrows have been created with line integral convolution of the velocity field and represent the mean velocity.

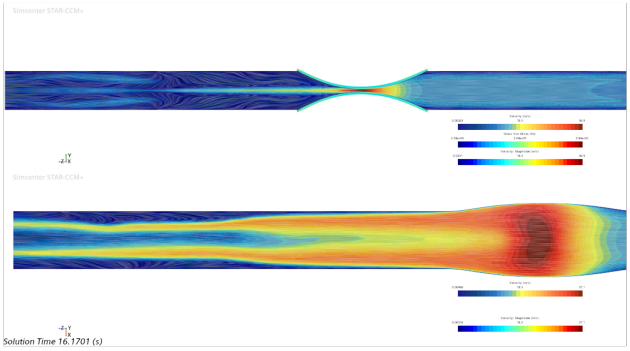

Figure 4.37: Mean axial velocity in the two main longitudinal cross sections of the domain at 16.17 seconds of the simulation. It can be seen in the side view that the jet flow in the middle becomes weaker. The arrows have been created with line integral convolution of the velocity field and represent the mean velocity.

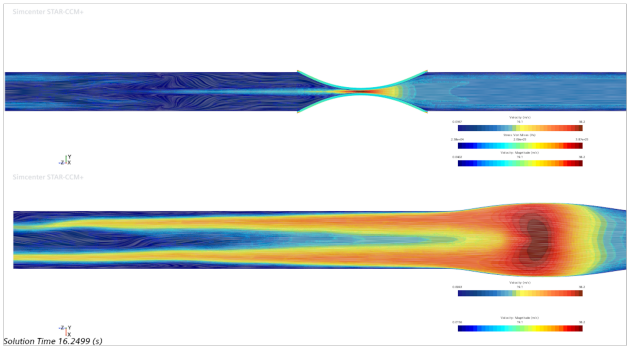

Figure 4.38: Mean axial velocity in the two main longitudinal cross sections of the domain at 16.25 seconds of the simulation. The twin jets at the downstream start to touch the walls. The arrows have been created with line integral convolution of the velocity field and represent the mean velocity.

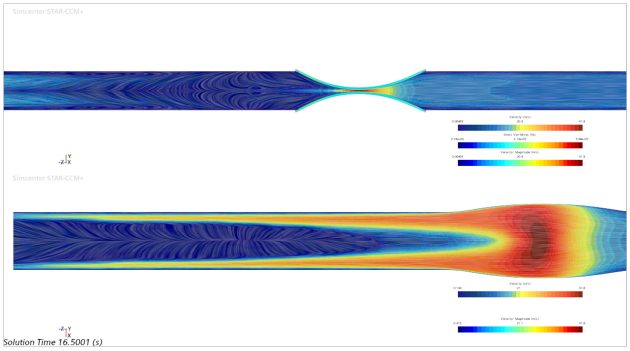

Figure 4.39: Mean axial velocity in the two main longitudinal cross sections of the domain at 16.5 seconds of the simulation. The twin jets at the downstream properly touch the walls. The arrows have been created with line integral convolution of the velocity field and represent the mean velocity.

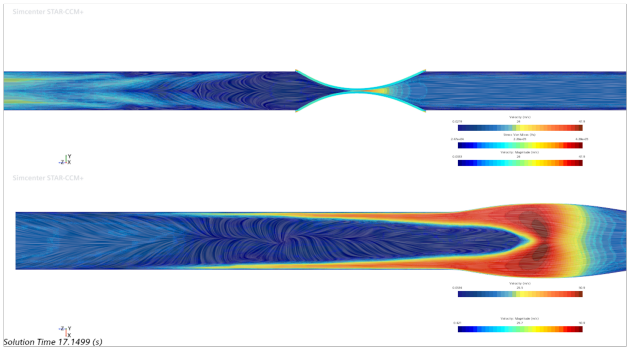

Figure 4.40: Mean axial velocity in the two main longitudinal cross sections of the domain at 17.15 seconds of the simulation (end of simulation). The twin jets at the downstream start to become weaker downwards, but more powerful at the contact point. The arrows have been created with line integral convolution of the velocity field and represent the mean velocity.

The flow pattern during an increase in external pressure at the tube is depicted in Figures 4.32 to 4.40. The first flow instability in the simulation occurs at 15.4 seconds. In Figure 4.32, the flow passes through the narrow neck of the tube, creating a single jet downstream like [64], [8],[5]. Vortices are visible at the outlet of the tube, and the size of the jet stream increases after these vortices, likely due to the vortices pushing more flow in the jet's direction. Similar patterns are observed at 15.5 seconds, but the jet stream becomes narrower. By 15.8 seconds, the jet stream straightens out and gradually increases in size compared to previous seconds.

In Figures 4.33 and 4.34, the flow is observed oscillating up and down along the zx axis. At 16 seconds (Figure 4.35), the flow starts to separate into two distinct flows, one moving up and the other down, like [5]. Additionally, it shows a decrease in the size of the jet compared to the previous time of the simulation. This indicates that as the tube's neck becomes narrower, the flow velocity increases, but less flow passes through.

At 16.087 seconds (4.36), oscillations with a dominant frequency of 164 Hz occur, causing the two flows on the zx-plane to start separating, while the jet stream becomes even smaller. By 16.17 seconds, the separation of the two flows becomes more apparent, and they are not symmetrical (Figure 4.37). Subsequently, the dominant frequency of the oscillations increases, the jet stream begins to disappear (Figure 4.38), and the two flows on the zx-plane touch the downstream walls.

As the tube becomes narrower and less flow passes through it, the length of the two jet streams on the zx-plane decreases (Figure 4.39), and the point where the two flows disconnect moves closer to the contact point of the tube walls. Ultimately, at 17.15 seconds (Figure 4.40, when the simulation diverges, the jet stream disappears, and there is a reverse flow. The separation point of the two jets is almost at the contact point.

From all of these figures, it can be seen that at 15.4 seconds, there is a small amount of reverse flow at the inlet of the flexible tube (Figure 4.32) from the beginning of the instability. While the external pressure increases, the lines of the reverse flow become denser as the tube becomes narrower and closer to the inlet. In this simulation, the Coandă effect found by Laudato cannot be observed because it is a symmetrical case [46],[47]. To capture an instability on the zy-plane, the simulation would have to be without symmetry as a boundary condition. Another thing worth mentioning is that, in this simulation, the jet flows on the zx-plane don't reconnect later at the downstream like in other experiments from the literature. This is probably because the length of the downstream is small. From this, it can be understood that the reconnection of the two jets has nothing to do with the onset of the oscillations of the tube.

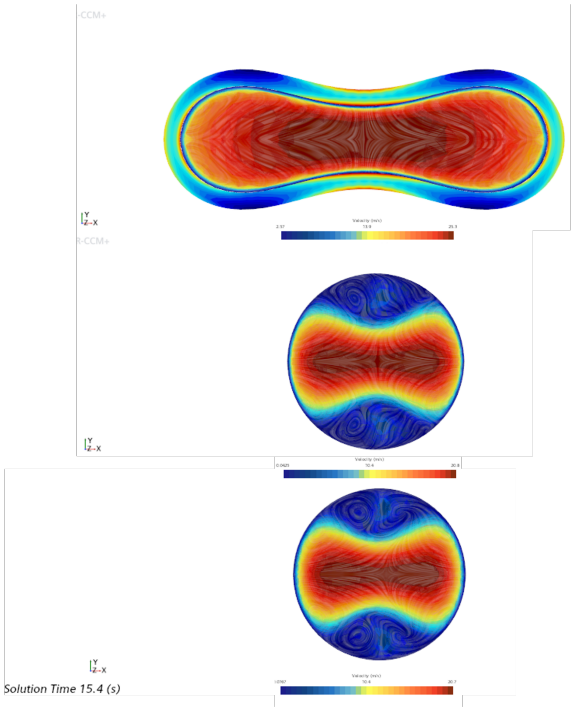

Figure 4.41: Mean axial velocity in the transversal cross section, outlet and after outlet of the domain respectively at 15.4 seconds of the simulation. At the outlet can be seen an asymmetric vortice. The arrows have been created with line integral convolution of the velocity field and represent the mean velocity.

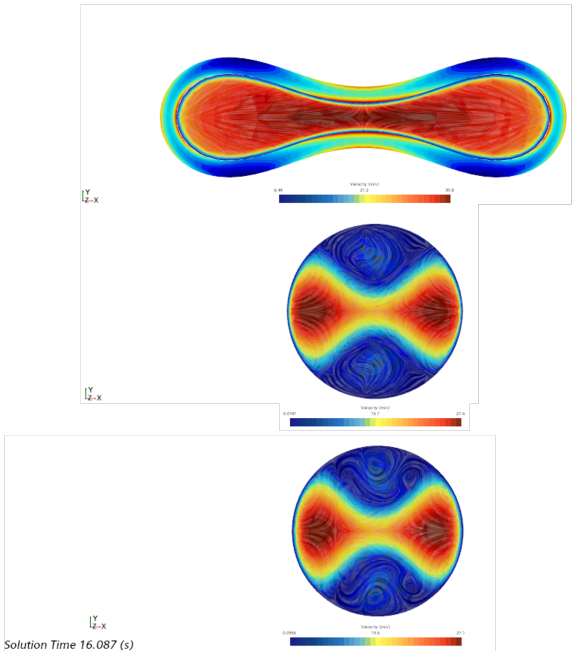

Figure 4.42: Mean axial velocity in the transversal cross section, outlet and after outlet of the domain respectively at 16.087 seconds of the simulation. The jet flow almost breaks to two. The arrows have been created with line integral convolution of the velocity field and represent the mean velocity.

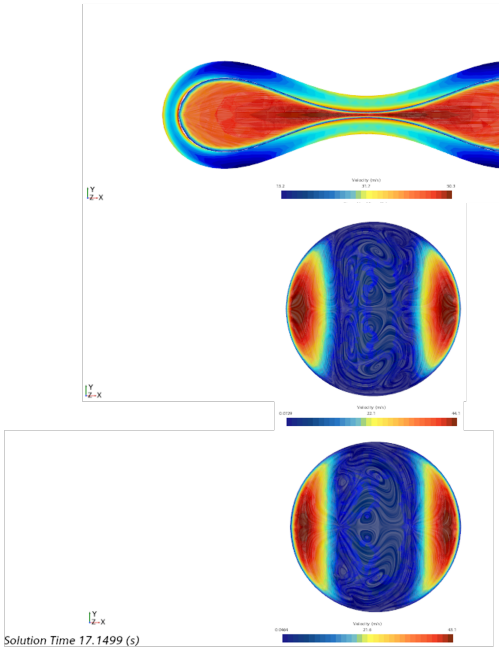

Figure 4.43: Mean axial velocity in the transversal cross section, outlet and after outlet of the domain respectively at 17.15 seconds of the simulation. The perpendicular velocity has increased and the flow hits the walls with bigger force. The arrows have been created with line integral convolution of the velocity field and represent the mean velocity.

In figures 4.41 - 4.43, the velocity field on the YX-plane in the mid-section of the tube, at the outlet, and downstream of the tube is shown for times 15.4, 16.087, and 17.15 seconds. Figure 4.41 indicates the presence of an asymmetrical vortex on the left and right sides, potentially causing the flow to lose its symmetry (Figure 4.29). Moreover, Figure 4.41 depicts the growth of this vortex, leading to clear asymmetry near the end of the downstream (Figure 4.29). All the figures show that the tube's walls are being pressed as external pressure increases. This results in a decrease in axial flow but an increase in perpendicular flow. Furthermore, the perpendicular flows on both sides hit the tube walls at approximately the same height as the walls contact point. As external pressure rises, the velocity of the perpendicular flow also increases, causing increased force on the tube walls, which may be crucial in understanding the onset of oscillations. Additionally, in Figure 4.42 at 16.087 seconds, two jet streams begin to separate, as previously described. Finally, in Figures 4.43, the now-separated jets touch the walls of the downstream.

Now some points have been placed at the downstream and where the two jet stream hit the wall, to check the frequencies of the flow.

The pressure points 4, 5, and 8 are located downstream from the outlet of the tube, while point 11 is positioned where the perpendicular flow hits the wall, close at the center of the flexible tube. The pressure fluctuations at these points are being analyzed using the FFT code. The time range for these FFT analyses is consistent at 16.087 - 16.17 seconds, during which the tube oscillates at a dominant frequency

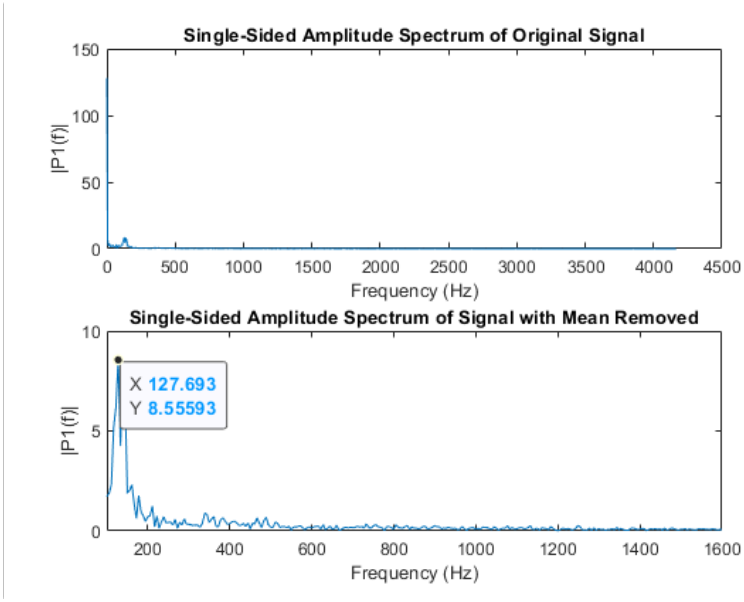

Figure 4.44: FFT for Pressure Point 4

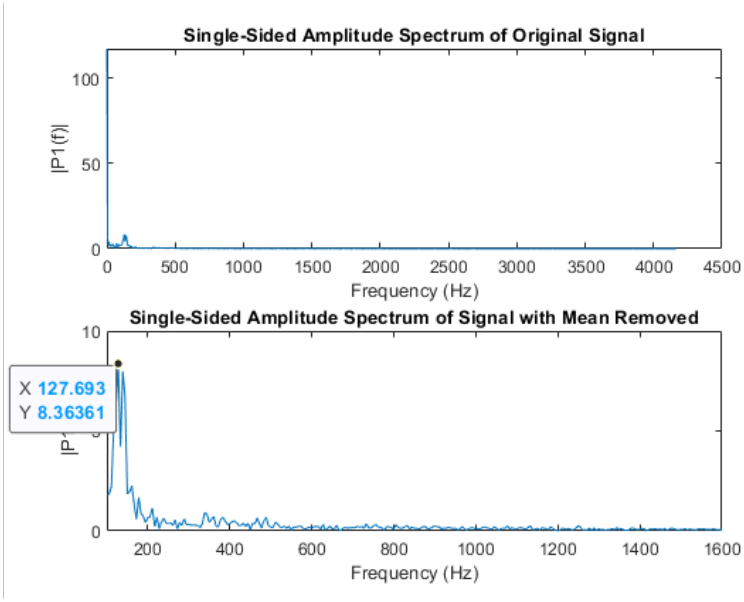

Figure 4.45: FFT for Pressure Point 5

of 164 Hz, as observed by Gregory. Figures 4.44 - 4.47 show that the frequency of the flow is 127 Hz, which is lower than the 164 Hz frequency. However, Figure 4.47 indicates that the fluid's frequency is 185 Hz, which is higher than 164 Hz. This suggests that the flow hitting the wall oscillates at a higher frequency than the tube, and then loses energy and oscillates at lower frequencies. These results indicate that the tube's oscillations may start from the impact of the perpendicular flow.

Now let's focus more at 15.4 seconds where the asymmetry of the downstream flow occurs. The Figure 4.48 indicates the the simulation converges towards a correct solution because it is adhering to the conservation of mass principle.

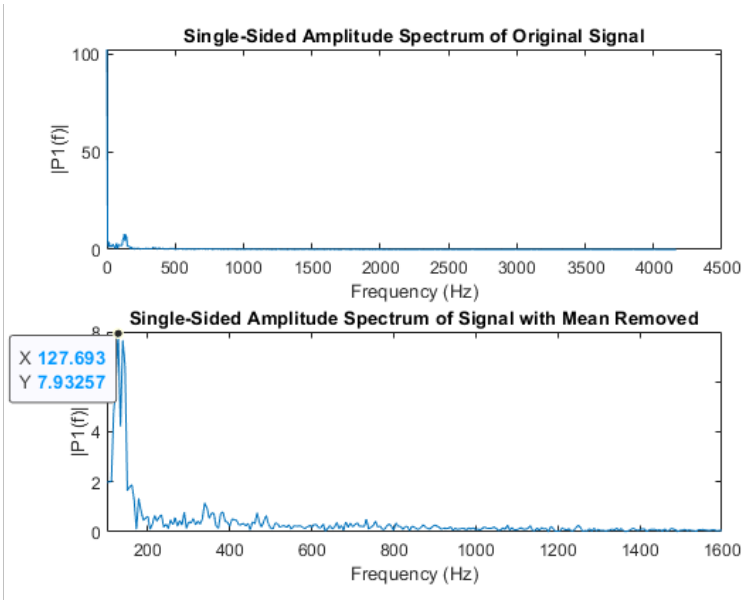

Figure 4.46: FFT for Pressure Point 8

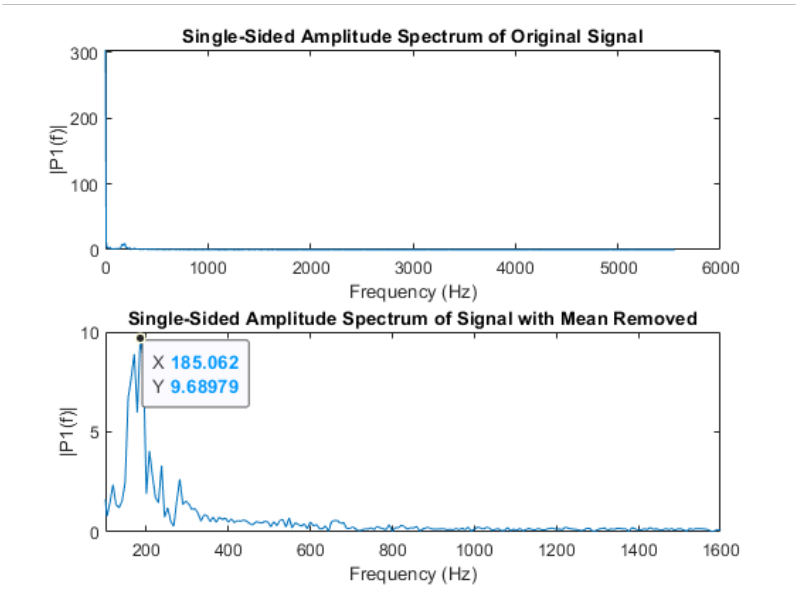

Figure 4.47: FFT for Pressure Point 11

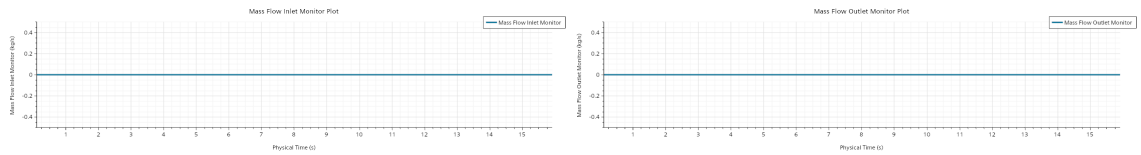

Figure 4.48: (a) Mass flow at the inlet of the tube (b) Mass Flow at the outlet of the tube

In order to understand why the flow breaks symmetry, we need to analyze the

pressure plots at three specific points: the mid-point, a point placed after the inlet and close to the tube wall, and a point before the outlet and close to the tube wall.

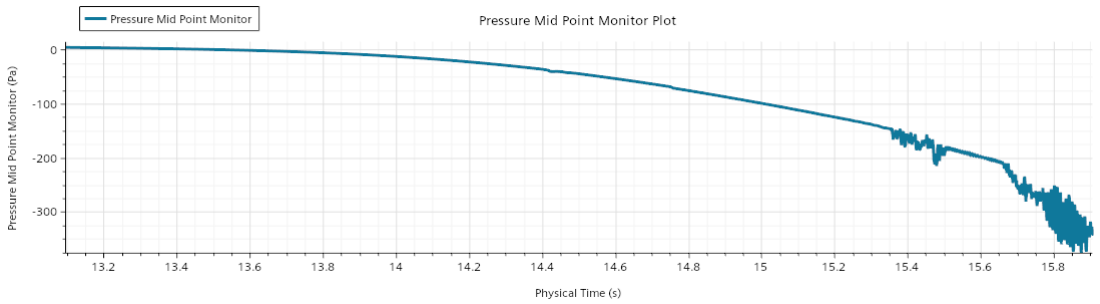

Figure 4.49: Pressure plot at mid point

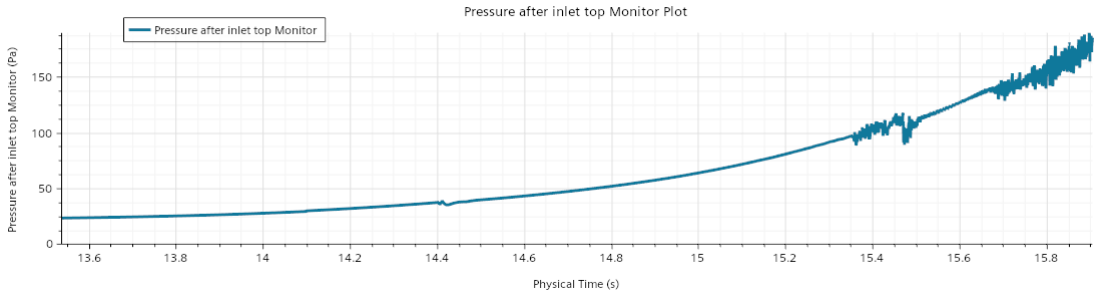

Figure 4.50: Pressure at a point placed after the inlet and close to the tube wall

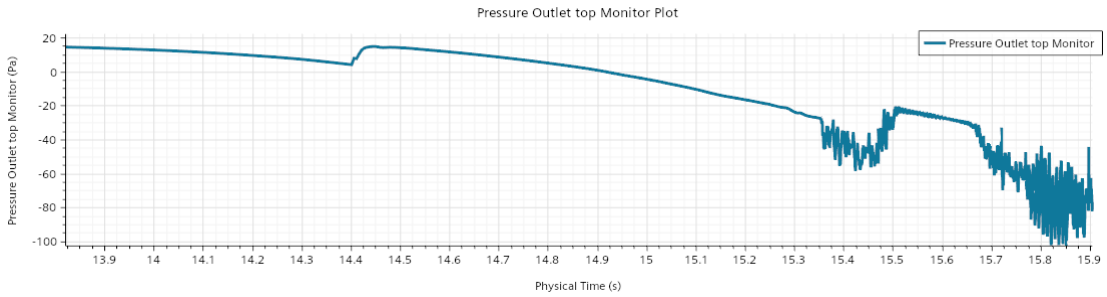

Figure 4.51: Pressure at a point before the outlet and close to the tube wall

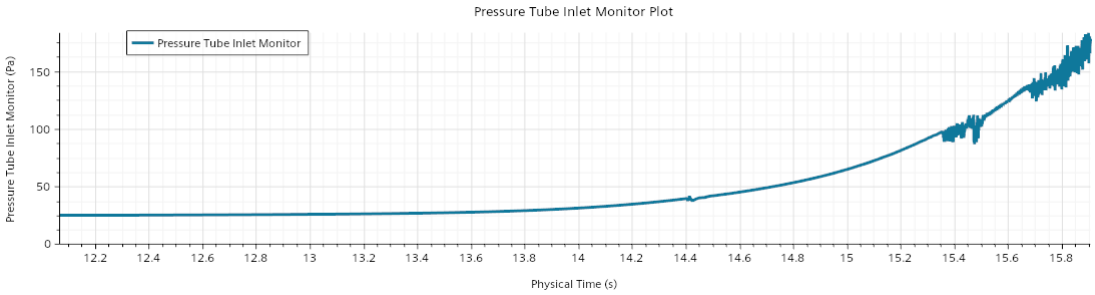

Figure 4.52: Pressure at the Inlet of the tube

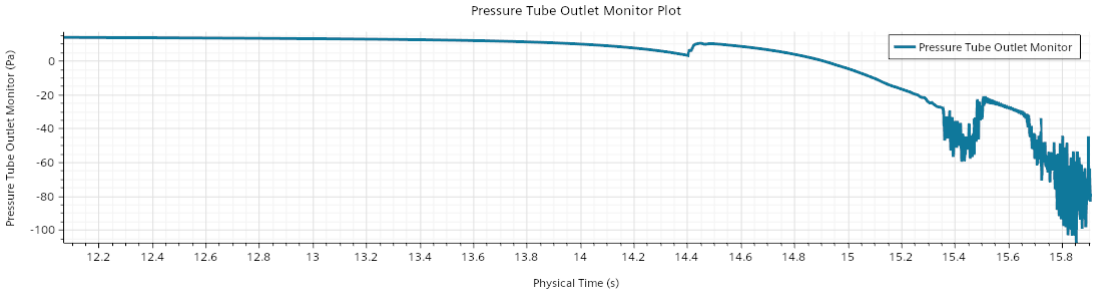

Figure 4.53: Pressure at the outlet of the tube

The pressure patterns from Figures 4.49 - 4.53 show that the pressure increases before the mid section of the tube and decreases at the mid section and outlet, like [47],[59],[5],[51]. The sudden peaks in the plots occur due to remeshing. In future research, it should be investigated how the remeshing impacts the simulation solution. Around 13.8 seconds, the pressures either start to decrease or increase, depending on the location. At this time, the external pressure is 1520 Pa. At 15.4 seconds, the pressure at the inlet of the tube is 100 Pa, and the pressure at the outlet is -43 Pa. All the pressure plots are decreasing very close to 15.4 seconds. At 13.3507 seconds, the pressure at the inlet starts to oscillate and decreases to very small values. The same happens for the rest of the pressure plots, with the oscillations starting at 13.3507 seconds. Generally, the amplitude of the pressure oscillations at 15.4 seconds is very small.

For the last part a cross correlation has been made between some pressure points of the fluid and points that are within tube walls.

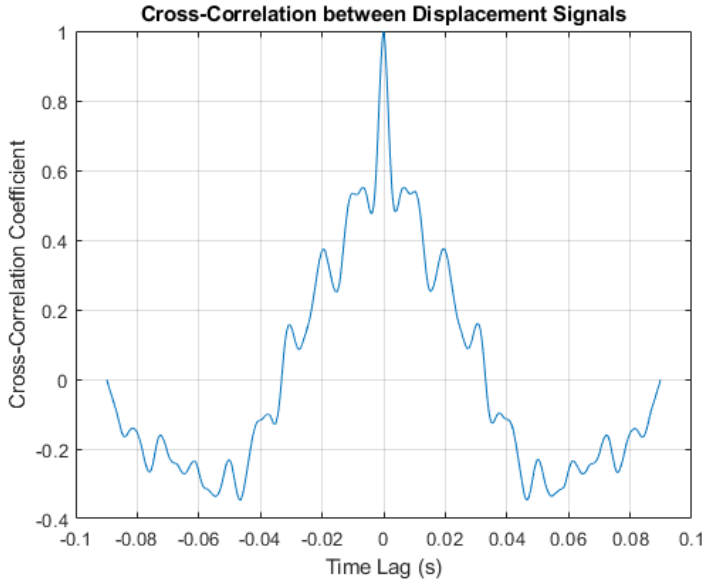

Figure 4.54: Cross Correlation of the displacement of the mid point with a point after midpoint within tube walls

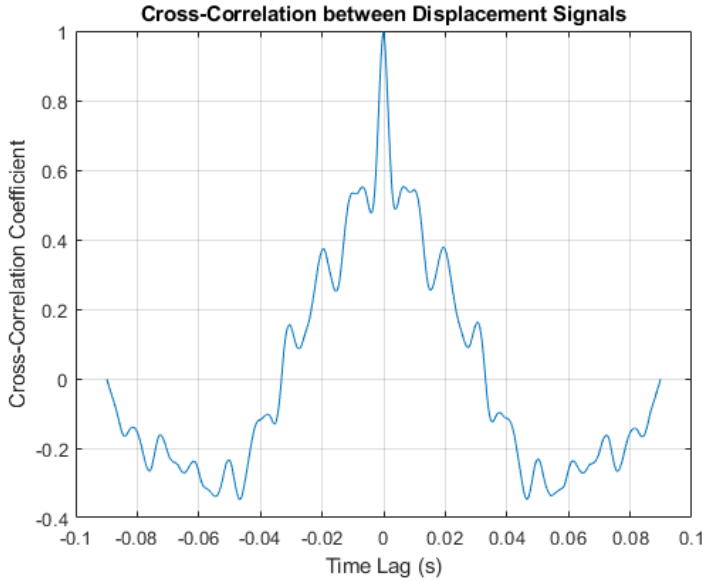

Figure 4.55: Cross Correlation of the displacement of the mid point with a point before midpoint within tube walls

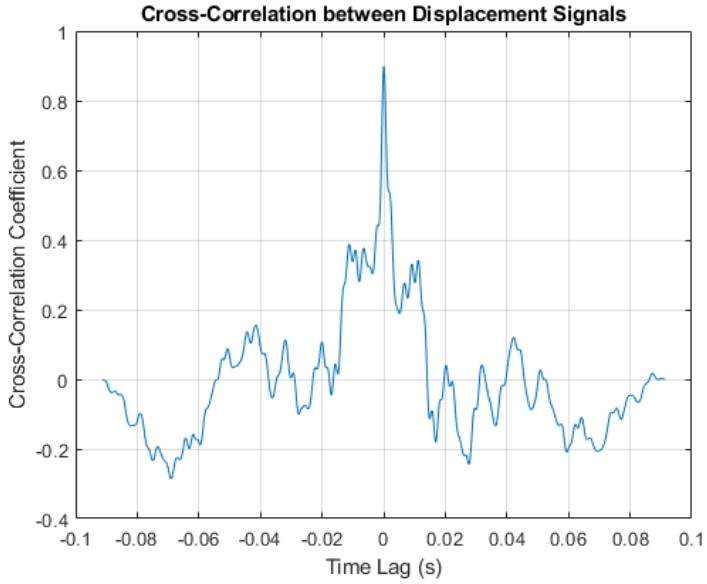

Figure 4.56: Cross Correlation of the pressure of two points after inlet

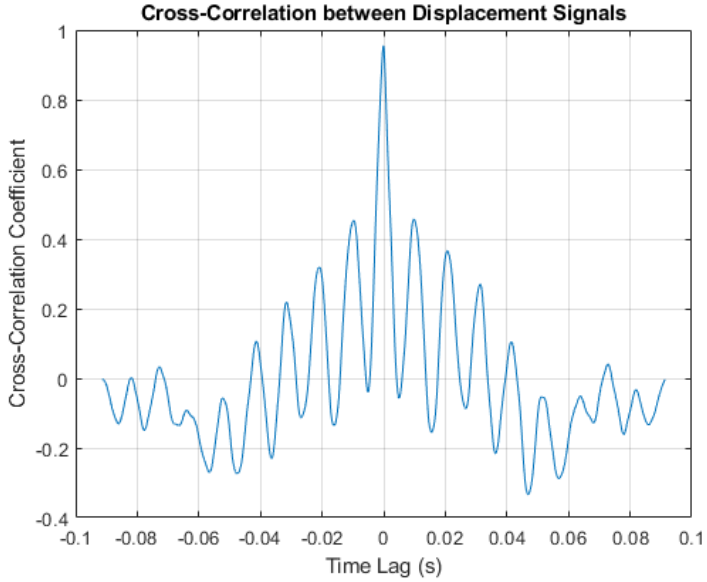

Figure 4.57: Cross Correlation of the pressure between a point after outlet and on much further after outlet

As can be seen from Figures 4.54 - 4.57 almost all the cross correlations are symmetrical. That indicates that the signal from both points is similar without any delay, so no waves can be seen. Only at Figure 4.56 a small delay can be observed which is the correlation between two points after the inlet, this delay might occur due to the vorticity or the reverse flow.

According to the above results a possible explanation for the mechanism of the oscillations is: As the tube's mid-section closes, the flow velocity increases, leading

to decreased pressure at the mid-section and outlet. Meanwhile, there's a reverse flow, increasing pressure at the inlet and creating vorticity before the tube's neck. This high vorticity could create eddies, adding to the main flow. Additionally, the increasing velocity at the middle causes the fluid to separate from the walls at the outlet, and the combination of these tow can break the symmetry at 15.4 seconds. The pressure that increases before the neck pushes the walls to open, and combined with the push of the perpendicular flow, the tube walls go against the external pressure until it's strong enough to push the walls back down, creating the oscillations. It's important to note that this explanation isn't definitive because it is uncertain about how the remesh affects these plots.

This is the first ever FSI case in literature that can simulate the wheezing with results that are close to reality. There are many improvements that can be made in future research. One is a more sophisticated mesh, with the use of turbulent models. Use the small time step 0.00003 second for the most time of the simulation to find the exact moment that the oscillations start and at what frequency the tube starts to oscillate. Use more LES instead of RANS to have more accurate results and capture the eddys and vortices that might occur.

5
Conclusion

The primary aim of this thesis was to develop a fluid-structure interaction (FSI) model to better understand the mechanism of wheezing at the human upper airways. In order to achieve this, a series of robust simulations have been carried out on diverse Starling resistor geometries, resembling the human upper airways where wheezing occurs. Following the validation of these simulations, they served as the foundation for constructing the new FSI model. Initially, an FSI simulation of the complete geometry without a pressure gradient was conducted and verified. Subsequently, the same scenario with a pressure gradient was executed, but the setup had to be modified due to the time-consuming nature of the simulation. The subsequent FSI simulation was identical and lacked a pressure gradient, but the geometry was divided in half and the simulation was made symmetrical. Following the validation of this scenario, the symmetrical FSI case with a pressure gradient was conducted, but due to instabilities during the tube's buckling state, a velocity inlet was used instead of a pressure inlet. Through these steps, this research has successfully developed the first-ever valid FSI simulation for modeling the onset of wheezing, uncovering the correlation between airway constriction, pressure dynamics, and oscillations.

The results of this research has shown that the FSI simulation can accurately capture the dominant frequency of 164 Hz of the tube's oscillations observed in the experiments. Furthermore the simulation has led to a new theory about the mechanism of the tube's oscillations behind wheezing. It is observed that the pressure at the inlet increases due to reverse flow and Bernoulli effect, while the pressure at the outlet decreases. This increase in inlet pressure generates vortices that induce instabilities near the tube wall. Additionally, the stenosis of the tube transversal velocity increases. The external pressure compresses the tube, but eventually, the rising pressure before and at the tube's neck forces the walls to open. This occurs repeatedly, and as the tube's neck narrows, both the velocities and instabilities increase, causing the tube to oscillate at higher frequencies. This affiriming the potential of FSI models in improving diagnosis and understanding complex mechanisms like the one behind wheezing.

In the future, there are several clear steps to take. One important area for improvement is refining the mesh of the fluid domain, using turbulence models, and finding a better strategy to trigger remeshing. Additionally, we should use LES instead of RANS to capture the vortices and eddies in detail. We should also employ more sophisticated techniques to analyze the frequencies of the oscillations, such as using wavelet analysis instead of FFT analysis to analyse frequencies over time. Lastly,

we can use the same setup to simulate real human upper airways that have been scanned with MRI and create a database with many simulations. This database can later be used to develop a medical instrument that helps doctors diagnose respiratory diseases in a cost-effective and efficient manner.

Bibliography

[1] A. L. Gregory, "A Theory for Wheezing in Lungs," 1 2019. [Online]. Available: https://www.repository.cam.ac.uk/handle/1810/284917

[2] A. Bohadana, G. Izbicki, and S. S. Kraman, "Fundamentals of lung auscultation," *The New England journal of medicine*, vol. 370, no. 8, pp. 744–751, 2 2014. [Online]. Available: https://pubmed.ncbi.nlm.nih.gov/24552321/

[3] N. A. Francis, H. Melbye, M. J. Kelly, J. W. Cals, R. M. Hopstaken, S. Coenen, and C. C. Butler, "Variation in family physicians' recording of auscultation abnormalities in patients with acute cough is not explained by case mix. A study from 12 European networks," *The European journal of general practice*, vol. 19, no. 2, pp. 77–84, 6 2013. [Online]. Available: https://pubmed.ncbi.nlm.nih.gov/23544624/

[4] B. Williams, M. Boyle, and P. O'Meara, "Can undergraduate paramedic students accurately identify lung sounds?" *Emergency medicine journal : EMJ*, vol. 26, no. 8, pp. 580–582, 8 2009. [Online]. Available: https://pubmed.ncbi.nlm.nih.gov/19625555/

[5] J. B. Grotberg and O. E. Jensen, "Biofluid mechanics in flexible tubes," *Annual Review of Fluid Mechanics*, vol. 36, pp. 121–147, 2004.

[6] C. D. Bertram, "Experimental Studies of Collapsible Tubes," pp. 51–65, 2003.

[7] O. E. Jensen, "Physiological Fluid Dynamics," Tech. Rep., 2003.

[8] M. Heil and A. L. Hazel, "Fluid-structure interaction in internal physiological flows," *Annual Review of Fluid Mechanics*, vol. 43, pp. 141–162, 1 2011.

[9] M. A. Burke, A. D. Lucey, R. M. Howell, and N. S. Elliott, "Stability of a flexible insert in one wall of an inviscid channel flow," *Journal of Fluids and Structures*, vol. 48, pp. 435–450, 2014. [Online]. Available: https://www.researchgate.net/publication/262021429_Stability_of_a_flexible_insert_in_one_wall_of_an_inviscid_channel_flow

[10] C. Davies and P. W. Carpenter, "Instabilities in a plane channel flow between compliant walls," *Journal of Fluid Mechanics*, vol. 352, pp. 205–243, 12 1997. [Online]. Available: https://www.cambridge.org/core/journals/journal-of-fluid-mechanics/article/abs/instabilities-in-a-plane-channel-flow-between-compliant-walls/16C4D1FB76D0E507E1B1C550A453B107

[11] L. Huang, "REVERSAL OF THE BERNOULLI EFFECT AND CHANNEL FLUTTER," *Journal of Fluids and Structures*, vol. 12, no. 2, pp. 131–151, 2 1998.

[12] P. S. Stewart, S. L. Waters, and O. E. Jensen, "Local instabilities of flow in a flexible channel: Asymmetric flutter driven by a weak critical layer," *Physics*

of Fluids, vol. 22, no. 3, pp. 2–18, 3 2010. [Online]. Available: /aip/pof/article/22/3/031902/256997/Local-instabilities-of-flow-in-a-flexible-channel

[13] Z. X. Cai and X. Y. Luo, "Self-excited oscillations in a fluid-beam collapsible channel," *ASME International Mechanical Engineering Congress and Exposition, Proceedings*, pp. 1243–1249, 2002. [Online]. Available: https://www.researchgate.net/publication/237426088_Self-Excited_Oscillations_in_a_Fluid-Beam_Collapsible_Channel

[14] F. Xu, J. Billingham, and O. Jensen, "Resonance-driven oscillations in a flexible-channel flow with fixed upstream flux and a long downstream rigid segment," *Journal of Fluid Mechanics*, vol. 746, pp. 368–404, 2014. [Online]. Available: https://www.cambridge.org/core/journals/journal-of-fluid-mechanics/article/abs/resonancedriven-oscillations-in-a-flexiblechannel-flow-with-fixed-upstream-flux-and-a-long-dow F66F2DB1EC9EB237922F8384F209BDA3

[15] X. Zhang, R. Ajaykumar, N. M. Sudharsan, and K. Kumar, "Investigation of two-dimensional channel flow with a partially compliant wall using finite volume-finite difference approach," *International Journal for Numerical Methods in Fluids*, vol. 49, no. 6, pp. 635–655, 10 2005. [Online]. Available: https://www.researchgate.net/publication/229430088_Investigation_of_two-dimensional_channel_flow_with_a_partially_compliant_wall_using_finite_volume-finite_difference_approach

[16] A. L. Gregory, A. Agarwal, and J. Lasenby, "An experimental investigation to model wheezing in lungs," *Royal Society Open Science*, vol. 8, no. 2, 2 2021.

[17] P. Forgacs, "Lung sounds," *British journal of diseases of the chest*, vol. 63, no. 1, pp. 1–12, 1969. [Online]. Available: https://pubmed.ncbi.nlm.nih.gov/4887198/

[18] N. Gavriely, T. R. Shee, D. W. Cugell, and J. B. Grotberg, "Flutter in flow-limited collapsible tubes: a mechanism for generation of wheezes," *Journal of applied physiology (Bethesda, Md. : 1985)*, vol. 66, no. 5, pp. 2251–2261, 1989. [Online]. Available: https://pubmed.ncbi.nlm.nih.gov/2745288/

[19] J. B. Grotberg and S. H. Davis, "Fluid-dynamic flapping of a collapsible channel: Sound generation and flow limitation," *Journal of Biomechanics*, vol. 13, no. 3, pp. 219–230, 1 1980.

[20] S. Standring, "Gray's anatomy : the anatomical basis of clinical practice," p. 1562, 2016. [Online]. Available: https://books.google.com/books/about/Gray_s_Anatomy.html?hl=el&id=LjP9rQEACAAJ

[21] H. H. Weitz and S. Mangione, "In defense of the stethoscope and the bedside," *The American journal of medicine*, vol. 108, no. 8, pp. 669–671, 2000. [Online]. Available: https://pubmed.ncbi.nlm.nih.gov/10856418/

[22] A. R. A. Sovijärvi, J. Vanderschoot, and J. E. Earis, "Standardization of computerized respiratory sound analysis," Tech. Rep., 2000. [Online]. Available: http://www.ilsa.cc/referenc.htm

[23] K. Staszko, C. Lincho, V. Engelke, N. Fiori, K. Silva, E. I. Nunes, and L. Zhang, "Pulmonary auscultation terminology employed in Brazilian medical journals between January of 1980 and December of 2003." *Jornal Brasileiro de Pneumologia*, 2006.

[24] A. J. Nunn and I. Gregg, "New regression equations for predicting peak expiratory flow in adults," *BMJ (Clinical research ed.)*, vol. 298, no. 6680, pp. 1068–1070, 1989. [Online]. Available: https://pubmed.ncbi.nlm.nih.gov/2497892/

[25] R. S. Raja, "Coupled fluid structure interaction analysis on a cylinder exposed to ocean wave loading," 2012. [Online]. Available: https://hdl.handle.net/20.500.12380/172681

[26] K. Bengtsson, "FSI-analysis on vibrations of a slender rod exposed to axial flow Calculations for nuclear power applications," Tech. Rep.

[27] J. Kesti and S. Olsson, "Master's Thesis: Fluid structure interaction analysis on the aerodynamic performance of underbody panels." Tech. Rep.

[28] Y. Bazilevs, K. Takizawa, and T. E. Tezduyar, "Computational Fluid-Structure Interaction: Methods and Applications," *Computational Fluid-Structure Interaction: Methods and Applications*, 12 2012.

[29] S. K. Chimakurthi, S. Reuss, M. Tooley, and S. Scampoli, "ANSYS Workbench System Coupling: a state-of-the-art computational framework for analyzing multiphysics problems," *Engineering with Computers*, vol. 34, no. 2, pp. 385–411, 4 2018.

[30] C. D. Bertram, C. J. Raymond, and K. S. Butcher, "Oscillations in a Collapsed-Tube Analog of the Brachial Artery Under a Sphygmomanometer Cuff," *Journal of Biomechanical Engineering*, vol. 111, no. 3, pp. 185–191, 8 1989. [Online]. Available: https://dx.doi.org/10.1115/1.3168364

[31] N. Gavriely, K. B. Kelly, J. B. Grotberg, and S. H. Loring, "Forced expiratory wheezes are a manifestation of airway flow limitation," *Journal of applied physiology (Bethesda, Md. : 1985)*, vol. 62, no. 6, pp. 2398–2403, 1987. [Online]. Available: https://pubmed.ncbi.nlm.nih.gov/3610933/

[32] F. G. Hoppin, J. M. Hughes, and J. Mead, "Axial forces in the bronchial tree," *Journal of applied physiology: respiratory, environmental and exercise physiology*, vol. 42, no. 5, pp. 773–781, 1977. [Online]. Available: https://pubmed.ncbi.nlm.nih.gov/863846/

[33] O. E. Jensen, "Instabilities of flows through deformable tubes and channels," Tech. Rep.

[34] T. J. Pedley and X. Y. Luo, "Modelling flow and oscillations in collapsible tubes," *Theoretical and Computational Fluid Dynamics*, vol. 10, no. 1-4, pp. 277–294, 1998. [Online]. Available: https://www.researchgate.net/publication/225711331_Modelling_Flow_and_Oscillations_in_Collapsible_Tubes

[35] H. F. Liu, X. Y. Luo, and Z. X. Cai, "Stability and pressure boundary conditions in the collapsible channel flows," *American Society of Mechanical Engineers, Pressure Vessels and Piping Division (Publication) PVP*, vol. 4, pp. 409–416, 2010. [Online]. Available: https://www.researchgate.net/publication/267611673_Stability_and_Pressure_Boundary_Conditions_in_the_Collapsible_Channel_Flows

[36] M. Heil and S. L. Waters, "Transverse flows in rapidly oscillating elastic cylindrical shells," *Journal of Fluid Mechanics*, vol. 547, pp. 185–214, 2006. [Online]. Available: https://www.researchgate.net/publication/30045779_Transverse_flows_in_rapidly_oscillating_elastic_cylindrical_shells

[37] ——, "How rapidly oscillating collapsible tubes extract energy from a viscous mean flow," *Journal of Fluid Mechanics*, vol. 601, pp. 199–227, 4 2008. [Online]. Available: https://www.researchgate.net/publication/231961008_How_rapidly_oscillating_collapsible_tubes_extract_energy_from_a_viscous_mean_flow

[38] R. J. Whittaker, M. Heil, O. E. Jensen, and S. L. Waters, "Predicting the onset of high-frequency self-excited oscillations in elastic-walled tubes," in *Proceedings of the Royal Society A: Mathematical, Physical and Engineering Sciences*, vol. 466, no. 2124. Royal Society, 12 2010, pp. 3635–3657.

[39] Huang, "Low Reynolds Number Turbulent FSI and its Applications in Biological Flows." [Online]. Available: https://doi.org/10.26190/unsworks/3993

[40] A. Marzo, X. Y. Luo, and C. D. Bertram, "Three-dimensional collapse and steady flow in thick-walled flexible tubes," *Journal of Fluids and Structures*, vol. 20, no. 6 SPEC. ISS., pp. 817–835, 2005.

[41] A. L. Hazel and M. Heil, "Steady finite-Reynolds-number flows in three-dimensional collapsible tubes," *Journal of Fluid Mechanics*, vol. 486, pp. 79–103, 7 2003.

[42] S. Zhang and H. Liu, "A FULLY-COUPLED THREE-DIMENSIONAL FLUID-STRUCTURE INTERACTION STUDY ON THE EXTERNALLY-PRESSURIZED COLLAPSIBLE TUBE AND THE INTERNAL FLOW," *Journal of Theoretical and Applied Mechanics (Poland)*, vol. 61, no. 2, pp. 395–406, 2023.

[43] P. S. Stewart, M. Heil, S. L. Waters, and O. E. Jensen, "Sloshing and slamming oscillations in a collapsible channel flow," *Journal of Fluid Mechanics*, vol. 662, pp. 288–319, 11 2010.

[44] B. Akbar, G. Johnsen, and P. R. Leinan, "Mathematical Modelling and Simulation of Flow in Collapsible Tubes," Tech. Rep., 2022.

[45] M. Laudato, R. Mosca, and M. Mihaescu, "Buckling critical pressures in collapsible tubes relevant for biomedical flows," *Scientific Reports*, vol. 13, no. 1, 12 2023.

[46] M. Laudato, E. Zea, E. Sundström, S. Boij, and M. Mihaescu, "Sound generation mechanisms in a collapsible tub," 1 2024. [Online]. Available: http://arxiv.org/abs/2401.02753http://dx.doi.org/10.1121/10.0026093

[47] K. Kounanis and D. S. Mathioulakis, "EXPERIMENTAL FLOW STUDY WITHIN A SELF OSCILLATING COLLAPSIBLE TUBE," *Journal of Fluids and Structures*, vol. 13, no. 1, pp. 61–73, 1 1999.

[48] C. D. Bertram and K. S. Butcher, "A collapsible-tube oscillator is not readily enslaved to an external resonator," *Journal of Fluids and Structures*, vol. 6, no. 2, pp. 163–180, 3 1992.

[49] C. D. Bertram and M. D. Sheppeard, "Interactions of pulsatile upstream forcing with flow-induced oscillations of a collapsed tube: mode-locking," *Medical engineering & physics*, vol. 22, no. 1, pp. 29–37, 1 2000. [Online]. Available: https://pubmed.ncbi.nlm.nih.gov/10817946/

[50] C. D. Bertram and R. J. Castles, "FLOW LIMITATION IN UNIFORM THICK-WALLED COLLAPSIBLE TUBES," *Journal of Fluids and Structures*, vol. 13, no. 3, pp. 399–418, 4 1999.

[51] K. Kumar and D. Prabhakaran, "Nonlinear oscillations of a collapsible tube subjected to unsteady external pressure," *Physics of Fluids*, vol. 34, no. 6, 6 2022.

[52] C. D. Bertram, N. K. Truong, and S. D. Hall, "PIV measurements of the flow field just downstream of an oscillating collapsible tube," *Journal of biomechanical engineering*, vol. 130, no. 6, 12 2008. [Online]. Available: https://pubmed.ncbi.nlm.nih.gov/19045540/

[53] C. D. Bertram and A. H. Nugent, "The flow field downstream of an oscillating collapsed tube," *Journal of biomechanical engineering*, vol. 127, no. 1, pp. 39–45, 2 2005. [Online]. Available: https://pubmed.ncbi.nlm.nih.gov/15868787/

[54] C. D. Bertram and J. Tscherry, "The onset of flow-rate limitation and flow-induced oscillations in collapsible tubes," *Journal of Fluids and Structures*, vol. 22, no. 8, pp. 1029–1045, 11 2006.

[55] J. W. Wang, Y. T. Chew, and H. T. Low, "Effects of downstream system on self-excited oscillations in collapsible tubes," *Communications in Numerical Methods in Engineering*, vol. 25, no. 5, pp. 429–445, 2009. [Online]. Available: https://www.researchgate.net/publication/227925460_Effects_of_downstream_system_on_self-excited_oscillations_in_collapsible_tubes

[56] T. B. Hoberg, E. Verneuil, and A. E. Hosoi, "Elastocapillary flows in flexible tubes," *Physics of Fluids*, vol. 26, no. 12, 12 2014. [Online]. Available: /aip/pof/article/26/12/122103/1013838/Elastocapillary-flows-in-flexible-tubes

[57] H. J. Wu, L. B. Jia, and X. Z. Yin, "Experiments on self-excited oscillation in a thin-walled collapsible tube," *Acta Mechanica Sinica/Lixue Xuebao*, vol. 31, no. 6, pp. 817–826, 12 2015. [Online]. Available: https://link.springer.com/article/10.1007/s10409-015-0465-y

[58] J. S. Zayko and V. V. Vedeneev, "Self-Exciting Oscillations of Elastic Tube Conveying Fluid at Laminar and Turbulent Flow Regimes," in *Journal of Physics: Conference Series*, vol. 894, no. 1. Institute of Physics Publishing, 10 2017.

[59] D. Yiasemides, A. Argyris, and D. S. Mathioulakis, "Transitory and Periodic Flow in a Self-Oscillating Collapsible Tube: Experimental Study," *Journal of Energy Engineering*, vol. 143, no. 4, 8 2017. [Online]. Available: https://www.researchgate.net/publication/315977536_Transitory_and_Periodic_Flow_in_a_Self-Oscillating_Collapsible_Tube_Experimental_Study

[60] V. E. NEGUS, "Humidification of the air passages," *Thorax*, vol. 7, no. 2, pp. 148–151, 6 1952. [Online]. Available: https://pubmed.ncbi.nlm.nih.gov/14931378/

[61] E. J. Chen, J. Novakofski, W. Kenneth Jenkins, and W. D. O'Brien, "Young's modulus measurements of soft tissues with application to elasticity imaging," *IEEE Transactions on Ultrasonics, Ferroelectrics, and Frequency Control*, vol. 43, no. 1, pp. 191–194, 1996. [Online]. Available: https://www.researchgate.net/publication/3260045_Youngs_Modulus_Measurements_of_Soft_Tissues_with_Application_to_Elasticity_Imaging

[62] Y. C. Fung and S. C. Cowin, "Biomechanics: Mechanical Properties of Living Tissues, 2nd ed." *Journal of Applied Mechanics*, vol. 61, no. 4, pp. 1007–1007, 12 1994. [Online]. Available: https://dx.doi.org/10.1115/1.2901550

[63] K. Horsfield and G. Cumming, "Morphology of the bronchial tree in man," *Journal of applied physiology*, vol. 24, no. 3, pp. 373–383, 1968. [Online]. Available: https://pubmed.ncbi.nlm.nih.gov/5640724/

[64] K. Ohba, K. Bando, A. Sakurai, Y. Tamura, and K. Itonaga, "Numerical Simulation and Experimental Verification of Wave Propagation in a Collapsible Tube," *JSME International Journal Series C Mechanical Systems, Machine Elements and Manufacturing*, vol. 42, no. 3, pp. 697–705, 9 1999.

[65] M. Heil and J. Boyle, "Self-excited oscillations in three-dimensional collapsible tubes: simulating their onset and large-amplitude oscillations," *Journal of Fluid Mechanics*, vol. 652, pp. 405–426, 2010. [Online]. Available: https://www.cambridge.org/core/journals/journal-of-fluid-mechanics/article/abs/selfexcited-oscillations-in-threedimensional-collapsible-tubes-simulating-their-onset-and-largean 1CDA82789EDEEEED182FF040F25002A3

[66] StarCCM+ Documentation, "Governing Equations," Tech. Rep., 2023.

[67] P. Steinmann, M. Hossain, and G. Possart, "Hyperelastic models for rubber-like materials: Consistent tangent operators and suitability for Treloar's data," *Archive of Applied Mechanics*, vol. 82, no. 9, pp. 1183–1217, 9 2012.

[68] StarCCM+ Documentation, "Fluid-Structure Interaction General Workflow Simcenter STAR-CCM+ 2302 User Guide," Tech. Rep.

[69] ——, "Fluid-Structure Interaction Reference Fluid Region > (and then)Interface Boundary > (and then)Physics Conditions FSI Coupling Specification," Tech. Rep.

[70] ——, "Load Stepping Simcenter STAR-CCM+ 2302 User Guide," Tech. Rep., 2023.

[71] ——, "Segregated Flow Solver," Tech. Rep.

[72] ——, "Fluid-Structure Interaction (FSI) Simcenter STAR-CCM+ 2302 User Guide," Tech. Rep., 2023.

[73] ——, "Morpher Motion Reference Morphing Motion Properties Morphing Order Simcenter STAR-CCM+ 2302 User Guide," Tech. Rep.

A

Appendix 1

A.0.1 Tube characteristics for two lobe buckling

This sections shows and discuss how the properties of the tubes can affect the two lobe buckling.

	0.99	0.98	0.97	0.96	0.95	0.94	0.93	0.92	0.91	0.9
Tube 1	×									
Tube 2	×									
Tube 3		×								
Tube 4	×									
Tube 5	×									
Tube 7						×				
Tube 8	×									
Tube 11										×

Table A.1: Tube Characteristics for Two Lobe Buckling

The same strategy and same mesh with Laudato has been used for all these various tubes to achieve two-lobe buckling. To accomplish this, all the tubes are elliptical rather than circular. Table A.1 displays that most of the tubes have a small axis radius that is 0.99 of the major axis radius. Exceptionally, tubes 3, 7, and 11 did not display similar behavior.

In table A.1, it is evident that tube 3 required a minor axis of 0.98 of the major radius, while tube 7 required 0.94 and tube 11 required 0.9. Explaining why tube 3 needs a smaller minor axis than the other tubes in the first category isn't straightforward, as it doesn't have any distinct characteristics. However, due to the locking of mesh cells, the tube buckles with 3 or even 4 lobes, as shown in the figure. The same situation applies to tube 7 and 11, which belong to the other two categories. All of them exhibited 3 or 4 lobes due to the locking. The simulations were repeated multiple times, confirming that the results are consistent and valid across all runs. This indicates that the properties of these tubes are more prone to locking of the cells and for creating more lobes during the buckling state. It could be suggested that tubes 7 and 11 are the most stretched tubes in their respective categories, so the stretched length L may be an important factor for the locking. Although this isn't the case for the first category, but tube 3 still only required 0.98 of the radius, which is very close to the rest of the tubes in its category.

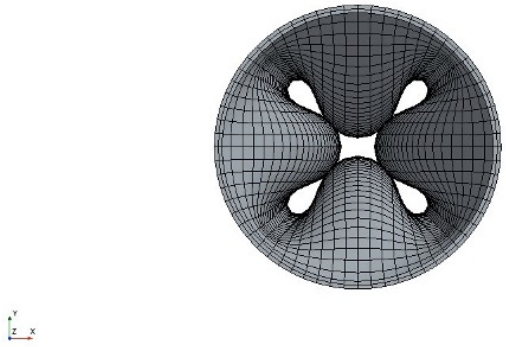

Figure A.1: 4 Lobes Buckling

The figure 4.10 a and b show the contact phase of tube 1 and tube 5. It can be observed that for thinner tubes like tube 5, the contact area is bigger than for thicker tubes like tube 1. This makes sense because thinner tubes are easier to deform, making them more flexible to external pressure. Unfortunately, this observation cannot be validated from Gregory's documentation, which is why only the tube laws have been used for validation. It is just an observation that might help future work.

Figure A.2: (a) Tube 1 Buckling State, (b) Tube 5 Buckling State

A.0.2 Frequency analysis of the tube's oscillations

Here is the table that shows the frequency analysis per simulation time. It includes the notes for each time and shows the trend of the oscillations dominant frequencies.

16 sec	6002	The oscillations start with peak to 133 then 148 and then 168
16.003 sec	6100	again same with 6200 but the 150 peak reach almost the 134 peak
16.0069 sec	6200	same with 6300
16.0099 sec	6300	same with 6500
16.012 sec	6400	at 6400 peak at 147 is almost the same with peak 134
16.015sec	6500	same pattern with 6700
16.0189sec	6600	same pattern with 6700, at 6600 the 168 peak is very close to the 134
16.0219sec	6700	same patter with the below 6850
16.024sec	6800	below 6850 we have peak at 134 then 142 and 168
16.0279sec	6900	below 7950 we have peak 142 then 125 and then 165
16.03sec	7000	below 7050 we have 133 peak then 145 and then 168
16.033sec	7100	peak 144 then 165 and then 124
16.036sec	7200	same with 7500, here below 7250
16.039sec	7300	same pattern with 7400 and below 7320 we have peak at 133 and then 147 and 166
16.042sec	7400	144 the highest, then 165 and then 133
16.045sec	7500	133 is the highest then 146 and then 165 below 7550
16.048sec	7600	almost same pattern with 7700, close to 7600 we have mostly 142 highest and 165-168 second
16.051sec	7700	biggest peak 147 then 132 and then 165-168 for all 100 timesteps
16.054sec	7800	peaks to 147-150 and some smaller to 164
16.057sec	7900	peaks to 147-150 and some smaller to 165
16.06sec	8000	mostly 148-150 Hz but there are time where we have peaks both 147-149 and 164-165 especially after 8050
16.063sec	8100	144-147 and 165-168 early 8100 mostly 165 and later we have 144-147
16.066sec	8200	147 -157
16.069sec	8300	165-168
16.072sec	8400	147 -157
16.075sec	8500	165-169
16.078sec	8600	165-169 second peak 145
16.081sec	8700	166 , second 145 third 186
16.084sec	8800	171 second 145
16.087sec	8900	165-169 early 8900 185 has the biggest peak close to 171
16.09sec	9000	174 and second 183 close to 9090
16.093sec	9100	same as 8900
16.096sec	9200	172
16.099sec	9300	169
16.102sec	9400	starts with 172 after 9470 we have 164 Peak
16.105sec	9500	165-169
16.108sec	9600	starts with 170 after 9620 we have 164 Peak
16.111sec	9700	165-170
16.114sec	9800	starts with 170 and goes to 164 close to 9900
16.117sec	9900	starts with 164 and goes to 170 close to 10000
	10000	same with 9800
	10100	same with 9900
	10200	same with 9800
	10300	same with 9900
	10400	same with 9800
	10500	same with 9900
	10600	same with 9800
	10700	same with 9900
	10800	same with 9800
	10900	same with 9900
	11000	same with 9800
	11100	same with 9900
	11200	same with 9800
	11300	same with 9900
	11400	same with 9800
	11500	same with 9900
	11600	same with 9800 the range starts to get bigger from 160 to 175
16.171sec	11700	same with 9900
	11800	from 175 goes to 198
	11900	from 200 to 180
	12000	from 180 to 200
	12100	211
	12200	186
	12300	150
	12400	200

Table A.2: Frequency analysis of the oscillations according to simulation time

DEPARTMENT OF SOME SUBJECT OR TECHNOLOGY
CHALMERS UNIVERSITY OF TECHNOLOGY
Gothenburg, Sweden
www.chalmers.se

CHALMERS
UNIVERSITY OF TECHNOLOGY